The Astrophysical Journal, 1002:59 (22pp), 2026 May 1 https://doi.org/10.3847/1538-4357/ae5b83
© 2026. The Author(s). Published by the American Astronomical Society.
OPEN ACCESS

XUE. Modeling MIR Molecular Gas Tracers of Truncation in Highly Irradiated Planet-forming Disks

Sebastian Hernández Arboleda[1], Germán Chaparro[1], Pablo Cuartas-Restrepo[1], Inga Kamp[2], María Claudia Ramírez-Tannus[3], Arjan Bik[4], Jenny Frediani[4], Thomas Haworth[5], Thomas Henning[3], Michael A. Kuhn[6], Thomas Preibisch[7], Bayron Portilla-Revelo[8,9], Elena Sabbi[10], Veronica Roccatagliata[11,12], Sierk E. van Terwisga[3], and Andrew Winter[5]

[1] FACom, Instituto de Física—FCEN, Universidad de Antioquia, Calle 70 No. 52-21, Medellín 050010, Colombia
[2] Kapteyn Astronomical Institute, Rijksuniversiteit Groningen, Postbus 800, 9700AV Groningen, The Netherlands
[3] Max-Planck Institut für Astronomie (MPIA), Königstuhl 17, 69117 Heidelberg, Germany
[4] Department of Astronomy, Stockholm University, AlbaNova University Center, SE-10691 Stockholm, Sweden
[5] Astronomy Unit, School of Physics and Astronomy, Queen Mary University of London, London E1 4NS, UK
[6] Centre for Astrophysics Research, Department of Physics, Astronomy and Mathematics, University of Hertfordshire, Hatfield, AL10 9AB, UK
[7] Universitäts-Sternwarte München, Ludwig-Maximilians-Universität, Scheinerstr. 1, 81679, München, Germany
[8] Department of Astronomy and Astrophysics, The Pennsylvania State University, 525 Davey Laboratory, University Park, PA 16802, USA
[9] Center for Exoplanets and Habitable Worlds, Penn State University, 525 Davey Laboratory, 251 Pollock Road, University Park, PA 16802, USA
[10] Gemini Observatory/NSFs NOIRLab, 950 N. Cherry Avenue, Tucson, AZ 85719, USA
[11] Alma Mater Studiorum, Università di Bologna, Dipartimento di Fisica e Astronomia (DIFA), Via Gobetti 93/2, 40129, Bologna, Italy
[12] INAF—Osservatorio Astrofisico di Arcetri, Largo E. Fermi 5, 50125, Firenze, Italy
Received 2025 July 26; revised 2026 March 25; accepted 2026 March 30; published 2026 April 24

Abstract

High-mass star-forming regions (SFRs), dominated by intense far-ultraviolet (FUV) radiation fields ($\sim 10^5\,G_0$) from nearby O stars, are the birthplaces of most planetary systems. While our understanding of protoplanetary disks (PPDs) and their evolution has primarily come from observations of isolated low-mass stars in the solar neighborhood, recent JWST observations of distant high-mass SFRs have provided new insights into the inner regions of the disks surrounding young stars. The impact of strong FUV irradiation on the structure and chemistry of PPDs remains poorly constrained. Here we use the thermochemical code `ProDiMo` to model how disk size and polycyclic aromatic hydrocarbon (PAH) abundance influence the infrared spectra of PPDs in high-mass SFRs. Our models explore taper radii from 5 to 70 au and PAH abundances from 10^{-4} to 10^{-2} relative to the interstellar medium, under both strong external irradiation ($10^5\,G_0$) and isolated conditions (G_0). We find that line-to-continuum ratios and integrated fluxes of key molecules, such as HCN and C_2H_2, decrease by up to 90% in the most compact, irradiated disks, indicating a strong dependence on disk truncation. PAH abundance primarily affects the continuum and PAH feature strengths in highly irradiated models. These results provide a framework for interpreting JWST spectra of PPDs in high-mass SFRs and underscore the critical roles of disk size and external FUV irradiation in shaping disk chemistry and evolution.

Unified Astronomy Thesaurus concepts: Protoplanetary disks (1300); Pre-main sequence stars (1290); Proplyds (1296); Polycyclic aromatic hydrocarbons (1280); Radiative transfer simulations (1967)

1. Introduction

The environment in which a protoplanetary disk (PPD) evolves plays a critical role in shaping its structural properties and chemical composition, both of which are essential for the planet formation process (A. Scally & C. Clarke 2001; S. Facchini et al. 2016; M. R. Bate 2018; A. J. W. Richert et al. 2018; A. J. Winter et al. 2018, 2024; R. J. Parker 2020; M. Reiter & R. J. Parker 2022; A. J. Winter & T. J. Haworth 2022; M. Allen et al. 2025). Recent studies have revealed a great diversity of disk morphologies and extrasolar planet systems (J. N. Winn & D. C. Fabrycky 2015; G. C. Molano et al. 2018; B. S. Gaudi et al. 2021), suggesting that each PPD exhibits unique characteristics that can significantly influence the final architecture of the forming planetary system (G. C. Molano et al. 2018; J. Salas et al. 2023). Although most star formation in the Universe occurs in high-irradiation environments (A. J. Winter & T. J. Haworth 2022), a significant amount of research on PPDs has focused on those in relatively quiet, low-mass star-forming regions (SFRs; C. Toci et al. 2023).

Observations of gas and dust in PPDs (e.g., A. Stolte et al. 2010; R. K. Mann et al. 2014; M. C. Ramírez-Tannus et al. 2023, 2025; O. Berné et al. 2024; T. Henning et al. 2024; C. E. Romero-Mirza et al. 2024) are crucial to understanding how the original chemical material from the cloud that gave rise to star−disk systems survives in sufficient quantities to impact the composition of the PPD and, eventually, the planets that form from it (B. Acke et al. 2010; K. I. Öberg et al. 2011; J. Aléon et al. 2022). In our solar system, comets and meteorites are remnants of this stage of planetary formation (J. J. Hester et al. 2004; D. Bockelée-Morvan et al. 2015), suggesting that PPDs undergo a chemical evolution that determines the local conditions for planet formation. G. Chaparro Molano & I. Kamp (2012a, 2012b) show how the environmental conditions within low-irradiation disks, those isolated or far away from the cores of massive SFRs, allow the formation of gaseous phase molecules such as H_2O, CO, CO_2, HCN, C_2H_2, CH_4, and H_2CO, among others.

Original content from this work may be used under the terms of the Creative Commons Attribution 4.0 licence. Any further distribution of this work must maintain attribution to the author(s) and the title of the work, journal citation and DOI.

The interaction between intense ultraviolet (UV) radiation and PPDs can significantly influence their evolution (S. Richling & H. W. Yorke 2000; V. Roccatagliata et al. 2011; M. Fang et al. 2012; F. Concha-Ramírez et al. 2019; R. J. Parker 2020; G. A. Coleman & T. J. Haworth 2022; L. Qiao et al. 2022; G. A. Coleman et al. 2024). Interactions between PPDs and nearby massive stars can lead to the truncation of their outer regions, due to photoevaporation thanks to the intense far-ultraviolet (FUV) and extreme-ultraviolet (EUV) radiation (D. Hollenbach et al. 1994; D. Johnstone et al. 1998; C. J. Clarke 2007; S. Pfalzner et al. 2014; A. J. Winter et al. 2018; F. Concha-Ramírez et al. 2019; R. B. Nicholson et al. 2019; M. Kuffmeier et al. 2020; R. J. Parker et al. 2021). Furthermore, the interaction between PPDs and their stellar environment can give rise to complex dynamical processes and complicate disk evolution, as stellar encounters could drastically affect the disk's morphology and dynamics (N. Cuello et al. 2018; E. C. Daffern-Powell et al. 2022) and leave an imprint on the mass and orbital parameters of forming planets (T. Kusaka et al. 1970; S. Desch 2007; J. Salas et al. 2023).

Observations of such environments are challenging owing to their significant distances, with many massive SFRs located more than 1.5 kpc away (e.g., E. D. Feigelson et al. 2013), and the high levels of extinction, which complicate observations using optical and near-infrared (NIR) telescopes. These sources are located at much greater distances than the low-to-intermediate-mass SFRs that have been studied so far (R. K. Mann et al. 2014; M. Ansdell et al. 2017, 2020; C. F. Manara et al. 2023; S. E. Van Terwisga & A. Hacar 2023). This has left a gap in our understanding of how the external environment affects disk evolution and planetary formation. Now, thanks to its unprecedented infrared sensitivity and angular resolution, JWST allows observations of the spectral characteristics of the inner part of such distant PPDs (E. F. van Dishoeck et al. 2023; M. C. Ramírez-Tannus et al. 2023, 2025).

In 2023, observations carried out by JWST using the MIRI-MRS (Medium Resolution Spectroscopy) instrument provided more detailed insights into the chemical composition of the inner regions of PPDs in highly irradiated environments (Section 2). To understand how these extreme conditions influence the spectral characteristics of PPDs, we describe in Section 3 how we developed our models and defined the parameter space. In Section 4, we quantify these effects. In Section 5, we present our discussion and suggestions for future work. Section 6 summarizes our findings.

2. Observational Insights into Disk Truncation in High-mass Star-forming Regions

Some observational evidence suggests that PPDs in highly irradiated environments exhibit signs of photoevaporation due to the FUV irradiation from nearby OB stars. This phenomenon has been observed in various locations, such as the Orion cluster (C. O'Dell et al. 1993; C. O'Dell & Z. Wen 1994; A. Scally & C. Clarke 2001; L. Ricci et al. 2008; R. K. Mann et al. 2014; R. D. Boyden & J. A. Eisner 2020; S. E. Van Terwisga & A. Hacar 2023; O. Berné et al. 2024; M.-L. Aru et al. 2024), the Arches cluster (A. Stolte et al. 2010), NGC 1977 (J. S. Kim et al. 2016), and the flame nebula NGC 2024 (T. J. Haworth et al. 2021). The photoevaporation process acts as a mechanism for disk truncation (F. C. Adams et al. 2004; A. J. Winter & T. J. Haworth 2022; G. A. Coleman & T. J. Haworth 2022; O. Berné et al. 2024; M. Gárate et al. 2024), limiting the disk sizes to the first tens of astronomical units (au), preserving the inner-disk structure and depleting the outer disk, which has consequences for giant planet formation (F. Concha-Ramírez et al. 2019)

The first MIRI-MRS observations of the inner disk of highly irradiated PPDs were presented by M. C. Ramírez-Tannus et al. (2023). They reported the presence of H_2O, CO, CO_2, HCN, and C_2H_2 in the XUE 1 system. The host star of XUE 1 is a solar analog located very close to the most massive stars in Pismis 24, showing that gas and dust in PPDs can survive in these environments. This work presented the first results from the eXtreme UV Environments (XUE) program using the JWST-MIRI instrument. The work took spectra of 12 potential PPDs around stars with spectral types from G to F, distributed in three subclusters in the NGC 6357 high-mass star-forming complex known to contain some of the most massive stars in our Galaxy (M. C. Ramírez-Tannus et al. 2025).

The line luminosities observed in XUE 1 are much lower than expected from thermochemical models of externally irradiated PPDs (M. A. Antonelli et al. 2014). Models predict that external irradiation increases the temperature of the upper layers of the disk, causing the emitting area of certain molecules to increase, boosting the line luminosity. However, this is not the case for XUE 1; therefore, M. C. Ramírez-Tannus et al. (2023) and B. Portilla-Revelo et al. (2025) suggest that the disk might be truncated, which reduces the emitting area of the XUE 1 and explains the lower luminosities for these chemical species. Here we explore the effect of the truncation radii (PPD size), the polycyclic aromatic hydrocarbon (PAH) abundances, and the external irradiation field on the H_2O, CO, CO_2, HCN, and C_2H_2 luminosities and the PAH feature strengths. PAH play an important role in highly irradiated environments, as they can influence the thermal and chemical processes, potentially affecting planet formation (K. Lange et al. 2021). The abundance of PAH in disks, which is currently very poorly known, can lead to important changes in the shape of the spectrum, especially in the continuum of these objects. When the PAH are externally irradiated, they act as a heating process, and their vibrational bands in the infrared will be very noticeable, affecting the continuum. PAH detections have been reported in some disks surrounding intermediate-to-low-mass stars, typically with abundances 2–3 orders of magnitude lower than the interstellar medium (ISM; V. C. Geers et al. 2006; B. Acke et al. 2010; S. Vicente et al. 2013; C. Joblin & A. G. G. M. Tielens 2020; P.-G. Valegård et al. 2021). These compounds can serve as tracers to understand the disk's chemistry, dynamics, and ionization state (W. Thi et al. 2019; G. A. Cruz-Diaz et al. 2020).

In the massive SFR M17 H II, M. S. Povich et al. (2007) demonstrated that PAH molecules can be efficiently destroyed by EUV and FUV photons. This result is consistent with chemical models by R. Visser et al. (2007) and with laboratory experiments performed by G. M. Caro et al. (2001). This photodestruction results in a reduced or even absent abundance of PAH in environments exposed to intense radiation fields. Observational support for this scenario is provided by the suppression of PAH features in the XUE sample (M. C. Ramírez-Tannus et al. 2025).

A more complete grid of physical–chemical disk models is necessary. This grid must involve a broad exploration of the parameters we have found to induce degeneracies in the physical modeling of the spectrum of these highly irradiated disks, such as the PAH abundance, the truncation radius, and

the external UV radiation field. In this way, synthetic spectra can be generated to aid in the interpretation of existing observations of other disks in the XUE sample and to guide future observation proposals with JWST-NIRSpec and JWST-MIRI-MRS, as well as the Atacama Large Millimeter/submillimeter Array and other ground-based observatories.

3. Models

We use the radiation thermochemical disk model ProDiMo (Revision: fd20eb05 2023/2/15; P. Woitke et al. 2009; I. Kamp et al. 2010, 2017; P. Woitke et al. 2016) to analyze how disk truncation ($R_{\rm taper}$) and PAH abundance ($f_{\rm PAH}$) influence the mid-infrared (MIR) spectra of externally irradiated PPDs. ProDiMo iteratively solves the chemistry, the thermal energy balance (including 2D dust continuum radiative transfer and gas heating/cooling processes), and the hydrostatic disk structure to self-consistently calculate the physical, thermal, and chemical disk structure (P. Woitke et al. 2009).

The code includes freezeout, desorption processes, PAH chemistry, and gas/dust thermal balance. The UV radiation field from external sources and the central object is propagated into the disk using multiwavelength radiative transfer, employing accelerated Λ iterations with long characteristics, and the diffusion approximation (P. Woitke et al. 2009; S. Antonellini et al. 2015).

ProDiMo also supports a parametric disk description. In this mode, the thermal gas balance and chemistry are iterated on a parameterized disk structure. This setup maintains the vertical structure across models, ensuring that the density profile remains identical in every case; this allows us to assess the impact of parameter variations ($R_{\rm taper}$, $f_{\rm PAH}$, and the external irradiation field) on PPD spectral properties.

In this work, for the heating and cooling processes and the thermal balance, we include molecules with relevant cooling lines in the 3–50 μm range to compare with the JWST spectra. Molecular data—such as energy levels, degeneracies, Einstein coefficients, line-center frequencies, and partition functions—are taken from F. Daniel et al. (2011) for H_2O; the LAMBDA database (F. L. Schöier et al. 2005) for CO, OH, and SiO; and the CHIANTI database (K. Dere et al. 1997) for C^+ and Si^+.

For the LTE calculation, we use the molecular data from HITRAN 2020. Table 1 lists the molecular data adopted (I. E. Gordon et al. 2022); other atomic and molecular species follow the standard ProDiMo setup (see P. Woitke et al. 2018). Additional species relevant for radiative heating and cooling via line absorption and emission are automatically included by ProDiMo but are not explicitly listed in Table 1 and in this section (see P. Woitke et al. 2009, 2011; I. Kamp et al. 2010). For chemical modeling, ProDiMo uses the UMIST 2006 database to take the rate coefficient R (J. Woodall et al. 2007), in combination with molecular self-shielding factors from the literature (see I. Kamp et al. 2010; P. Woitke et al. 2019).

To compute the emission spectrum of each molecule, ProDiMo can perform LTE and non-LTE calculations; in this work, we focus on the LTE treatment. For the non-LTE treatment, ProDiMo employs an escape probability approach to determine the level populations, based on the calculated molecular column densities and continuum radiative transfer. Thus, dust IR pumping of the disk level populations is fully taken into account (P. Woitke et al. 2018).

Table 1
Selected MIR Molecules Included in the Heating and Cooling Processes

Species	λ (μm)	No. Levels	No. Lines
CO_2	[3–20]	252	126
C_2H_2	[11–17]	22034	11017
HCN	[11–17.5]	252	126
CH_4	[12–25]	1532	766
OH	[10–50]	2530	1265
NH_3	[9–50]	6062	3031
H_2CO	[9–50]	3134	1567
CH_3OH	[9–50]	28570	14285
CS	[9–50]	14	7
SO_2	[6–12]	290924	145462
H_2S	[6–12]	1092	546
NO	[9–50]	364	182

Note. All available levels and lines are included from the HITRAN 2020 database (I. E. Gordon et al. 2022) within the listed wavelength intervals.

In the following sections, we first outline the fiducial model setup for each simulation series (Section 3.1). The parameter space and the full set of models are presented in Section 3.2. Finally, Section 3.3 details the specific set of species that we follow to examine the influence of our parameter space on the intensity of their MIR spectra.

3.1. Fiducial Model

To define the fiducial model, we computed two hydrostatic equilibrium models under different levels of external UV irradiation field (χ). These hydrostatic models serve exclusively to derive the vertical structure parameters—as described below—which are then used to define a fixed, parameterized density disk structure for all subsequent models in our grid.

One model is exposed to extreme external irradiation with $\chi = 10^5 G_0$, while the other is not externally irradiated ($\chi = G_0$), where G_0 is the Habing field ($G_0 = 1.6 \times 10^{-3}$ erg cm^{-2} s^{-1}). In both models, we adopt a taper radius $R_{\rm taper} = 70$ au, which marks the location where the gas surface density transitions to an exponential decline with tapering exponent $\gamma = 1.0$ (Table 2). With this choice of $R_{\rm taper}$, the resulting outer radius of the disk is approximately 500 au, consistent with the upper end of outer radii measured for isolated PPDs in observations (J. P. Williams & L. A. Cieza 2011). The models also assume a PAH abundance relative to the ISM, $f_{\rm PAH} = 10^{-2}$. In ProDiMo, the ISM PAH abundance is taken to be 3×10^{-7} relative to hydrogen nuclei, which is a typical value for PPDs around low- and intermediate-mass stars (V. C. Geers et al. 2006; A. G. Tielens 2008; C. Joblin & A. G. G. M. Tielens 2020). The properties of the central object and the disk's inclination were set as reported by M. C. Ramírez-Tannus et al. (2023) and B. Portilla-Revelo et al. (2025) for the XUE 1 source (see Table 2). We aim to simulate T Tauri stars with similar spectral types and luminosities.

For the dust population, ProDiMo adopts a power-law size distribution $f_0(a)$ as a function of the particle radius a [cm], given by $f_0(a) \propto a^{-a_{\rm pow}}$ over the interval $a_{\rm min} = 0.05$ μm to $a_{\rm max} = 3000$ μm (see Table 2). We selected this size range because PPD dust is predominantly composed of micrometer-sized grains and millimeter-sized particles are observed at millimeter wavelengths (C. Lefèvre et al. 2014; P. Woitke et al. 2016; N. P. Ballering et al. 2023).

Table 2
Simulation Parameters ($\chi = G_0$ and $\chi = 10^5\ G_0$ Models)

Component	Parameter	Value
Central object	Luminosity ($L_\star$)[a]	3.3 $L_\odot$
	Mass ($M_\star$)[a]	1.1 $M_\odot$
	$T_{\rm eff}$[a]	4600 K
	Distance	400 pc
Disk structure	Disk mass ($M_{\rm disk}$)	Varied[b]
	Inner radius ($R_{\rm in}$)	0.05 au
	Taper radius ($R_{\rm taper}$)	Varied[b]
	Outer radius ($R_{\rm out}$)	Varied[b]
	Reference scale height (H_0)	0.0258 au
	Reference radius (R_0)	1 au
	Flaring power index (β)	1.2
	Power index of vert. col. dens. (ϵ)	1.0
	Tapering-off exponent (γ)	1.0
	Inclination[a]	60°
PAH	PAH abundance relative to ISM ($f_{\rm PAH}$)	Varied[b]
Dust properties	Dust-to-gas mass ratio (ρ_d/ρ)	0.01
	Minimum dust particle radius ($a_{\rm min}$)	0.05 μm
	Maximum dust particle radius ($a_{\rm max}$)	3000 μm
	Dust size distribution power index ($a_{\rm pow}$)	3.5
	Dust material mass density ($\rho_{\rm gr}$)	2.09 g cm^{-3}
Grid resolution	Number of radial grid points [$N_{\rm XX}$]	120
	Number of vertical grid points [$N_{\rm ZZ}$]	120

Notes.
[a] XUE 1 parameters for the central object.
[b] Refer to Table 3.

As mentioned above, parameterized models allow us to fix the disk's 2D gas density profile by prescribing the scale height H as a function of radius r. This approach isolates the effects of the taper radius ($R_{\rm taper}$) and PAH abundance ($f_{\rm PAH}$) on the disk temperature and chemistry while keeping the density structure identical across all models. This requires computing the scale height at each radius using

$$\rho(r, z) = \rho_0 \exp\left(-\frac{z^2}{2H^2}\right), \quad (1)$$

where z is the vertical distance from the midplane, $\rho(r, z)$ is the gas volume density, and $\rho_0 \equiv \rho(r, 0)$ is the midplane gas density. To derive the scale height H from the hydrostatic models, we computed, at each radius, the value of z for which the gas volume density decreases to 60% of the midplane gas density ($H(r)$). From Equation (1), when $z = H$, the gas volume density satisfies $\rho(r, z) \approx 0.6\,\rho_0$. We then fitted a power law to the resulting $H(r)$ profile to determine the flaring index β and the scale height (H_0) at the reference radius of $R_0 = 1$ au, thereby parameterizing the vertical disk structure as

$$H(r) = H_0\left(\frac{r}{R_0}\right)^{\beta}. \quad (2)$$

The flaring index calculated for both models is approximately $\beta \approx 1.2$, with a scale height of $H_0 \approx 0.0258$ au at the reference radius. It is important to note that this definition of $H(r)$ is based on a fixed density threshold (60% of the midplane density, as mentioned above; P. Woitke et al. 2009), which makes the derived flaring index relatively insensitive to changes in the thermal structure driven by external irradiation. As a result, both hydrostatic models yield similar values of β and H_0, even under very different irradiation conditions.

Subsequently, we performed new simulations using the derived values of β and H_0, following the parametric prescription described above. This procedure establishes a standardized disk structure for all subsequent models within the parameter space (χ, $R_{\rm taper}$, and $f_{\rm PAH}$), as shown in the gas density profile (Appendix A).

Table 3
Summary of the Parameter Space Explored in the Two Model Series

$R_{\rm taper}$ (au)	$M_{\rm disk}$ ($M_\odot$)	$R_{\rm out}$ (au)	$f_{\rm PAH}$ Relative to ISM		
			10^{-4}	10^{-3}	10^{-2}
70	0.01	477	X0R70f1e-4	X0R70f1e-3	X0R70f1e-2
			X5R70f1e-4	X5R70f1e-3	X5R70f1e-2
15	0.002	122	X0R15f1e-4	X0R15f1e-3	X0R15f1e-2
			X5R15f1e-4	X5R15f1e-3	X5R15f1e-2
5	0.0007	46	X0R5f1e-4	X0R5f1e-3	X0R5f1e-2
			X5R5f1e-4	X5R5f1e-3	X5R5f1e-2

Each model is labeled as XIRIIfIII, where I represents the log value of the external irradiation field, II the taper radius in au, and III the abundance of PAH relative to the ISM. For example, X5R15f1e-3 corresponds to a model with an external irradiation field of $\chi = 10^5\ G_0$, a taper radius of $R_{\rm taper} = 15$ au, and a PAH abundance of $f_{\rm PAH} = 10^{-3}$. The disk parameter $M_{\rm disk}$ is adjusted accordingly for each model. The outer radius ($R_{\rm out}$) is defined as the radius where the surface density column drops to $N_{<\rm H>,ver} = 10^{20}$cm^{-2}.

3.2. Parameter Space

To explore the effects of different truncation radii on spectral characteristics in irradiated PPDs, we adjusted the taper radius ($R_{\rm taper}$), simulating different truncation radii. Table 3 lists all models and their simulated disk sizes.

To ensure consistent gas density distributions across disk sizes, we keep the density constant over the first tens of au, and any radial extension of the disk adds mass. To achieve this, we adjust the disk mass ($M_{\rm disk}$) for each truncation radius following P. Woitke et al. (2009):

$$M_{\rm disk} = 2 \times 2\pi \int \Sigma(r) r \quad dr, \quad (3)$$

where the factor of 2 accounts for the symmetry with respect to the midplane, r is the radius, and $\Sigma(r)$ is the gas surface density in g cm^{-2}. The surface density is assumed to follow a radial power law with index ϵ, modified by an exponential tapering characterized by γ (P. Woitke et al. 2016),

$$\Sigma(r) \propto r^{-\epsilon} \exp\left(-\left(\frac{r}{R_{\rm taper}}\right)^{2-\gamma}\right). \quad (4)$$

As shown in Figure A1, the gas density distribution remains consistent across all models. Table 3 summarizes the disk masses for each taper radius, and Figure 1 shows the universal radial gas surface density profile (Σ_g), which is common to all models at a given disk size.

To evaluate the impact of PAH abundance on the spectra of externally irradiated PPDs, we explore a parameter space that includes a nominal ISM-relative abundance ($f_{\rm PAH} = 10^{-2}$), followed by progressively lower values in subsequent models.

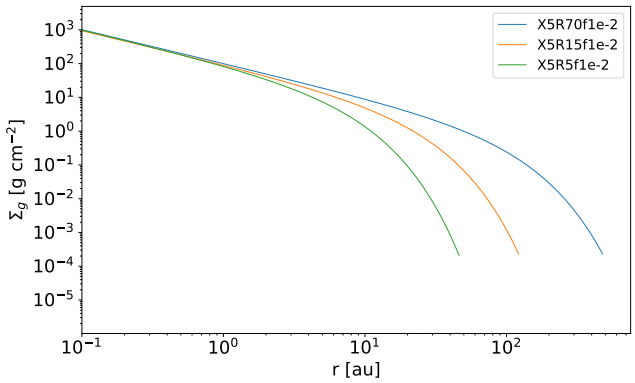

Figure 1. Gas surface density profile for models with different $R_{\rm taper}$, illustrating the parameterized disk structure. All models with the same disk size share an identical gas surface density profile.

The decrease in $f_{\rm PAH}$ reflects the expected PAH destruction under strong external UV irradiation (G. M. Caro et al. 2001; R. Visser et al. 2007) and is consistent with the absence of PAH features in the XUE sample (M. C. Ramírez-Tannus et al. 2025); only the XUE 10 object shows evidence of the 6.2 and 11.2 μm feature (J. Frediani et al. 2025).

We calculated a $2 \times 3 \times 3$ grid of models (χ, $R_{\rm taper}$, $f_{\rm PAH}$) for which we summarized the fixed parameters in Table 2 and the variable parameters and model names in Table 3.

3.3. Species Selection

To be able to connect our results directly to the MIRI-MRS observations from JWST, we have selected species detected in XUE 1 (M. C. Ramírez-Tannus et al. 2023; B. Portilla-Revelo et al. 2025) and commonly detected in nearby PPDs (e.g., Á. Kóspál et al. 2023; M. J. Colmenares et al. 2024; T. Henning et al. 2024; A. Banzatti et al. 2025): H_2O, CO, CO_2, HCN, and C_2H_2. Table 4 summarizes the molecules and the MIR spectral range analyzed. Our objective is to quantify the flux continuum ratio of these species across the parameter space and to explore the emission regions for each molecule.

4. Results

To understand the effect of the disk size and PAH abundance on continuum emission and the molecular features, we generated synthetic spectra for all models across the wavelength range of 5–28 μm, aligning with the capabilities of the MIRI-MRS instrument. To quantify the continuum emission, we present the spectral energy distribution (SED) and measure the spectral index between 18 and 27 μm, as this wavelength range is a good tracer of the optically thick disk continuum emission (E. Furlan et al. 2009), without the potential contamination from PAH emissions in all our models. We compute the molecular flux per molecule across all models to evaluate the impact on line strength emissions for the selected species, and we present synthetic spectra for each species. Furthermore, we present the emission regions associated with the strongest emission lines from some species, shedding light on how our parameter space influences the disk structure and providing deeper insights into the measured integrated fluxes.

Table 4
Selected Molecules and Their Spectral Ranges in the Mid-IR Region Used in This Study

Species	λ (μm)	No. Lines
CO	[4.9–5.1]	17
H_2O	[6.41–7.22]	494
HCN	[11.9–16.5]	118
C_2H_2	[12.2–15.5]	10679
CO_2	[13.5–16.5]	125
H_2O	[13.5–17.25]	310

4.1. Continuum Analysis

The truncation radius has a significant effect on the intensity of continuum emission, as demonstrated by A. J. W. Richert et al. (2015). They show that within the 3–8 μm range of the Spitzer/IRAC bands the infrared excess is sensitive to disk size. In our study, larger disks ($R_{\rm taper} = 70$ au) exhibit a more pronounced excess in the MIR to far-infrared (FIR) regions. This effect becomes even more evident when the disk is subjected to higher external irradiation, as shown in the synthetic spectra (Figure 2) and the continuum SED (Figure 3).

This behavior is consistent with the dust temperature structure (Figure C1). In both model series (isolated and externally irradiated disks), the inner dust temperature dominates the NIR spectrum: for all cases, temperatures at $r < 0.2$ au reach $\geqslant$500 K, which explains the weak sensitivity of the NIR continuum to our parameter space. By contrast, in the MIR to FIR, the taper radius $R_{\rm taper}$ and the external irradiation field χ play a dominant role. Increasing the disk size expands the region where the dust temperature is $\sim$ 200 K, whereas external irradiation elevates the dust temperature in the outer disk by $\sim$50 K near the midplane and by a few hundred kelvin in the upper layers. Together, these effects enhance the MIR to FIR emission.

4.1.1. Spectral Index

To quantify how our parameter space affects the continuum emission, we measure the SED slope between 18 and 27 μm using the spectral index defined by E. Furlan et al. (2009),

$$\eta_{18-27} = \frac{\log_{10}(\lambda_{27} F_{27}) - \log_{10}(\lambda_{18} F_{18})}{\log_{10}(\lambda_{27}) - \log_{10}(\lambda_{18})}. \quad (5)$$

We use here F_{18} and F_{27}, the fluxes at 18 and 27 μm, respectively, in erg s^{-1}cm^{-2}Å^{-1}. We selected these wavelengths as the endpoints for the slope determination because they probe the long-wavelength continuum emission from the optically thick disk (E. Furlan et al. 2009), are sensitive to the dust temperature—thereby tracing the influence of external irradiation and disk geometry (i.e., disk size)—and are free from contamination by PAH emission features (Figure 3).

As shown in Figure 4, externally irradiated models exhibit higher spectral indices than their isolated counterparts, reflecting the effect of external irradiation on the dust temperature (Appendix C) and the corresponding excess in the MIR to FIR region (Figure 2). This effect is more pronounced for larger taper radii (70 au), where the absolute difference in the spectral index η_{18-27} between the two model series is approximately 3. For the smallest taper radius (5 au), the difference is only about 0.4 (see Figure 4), illustrating how

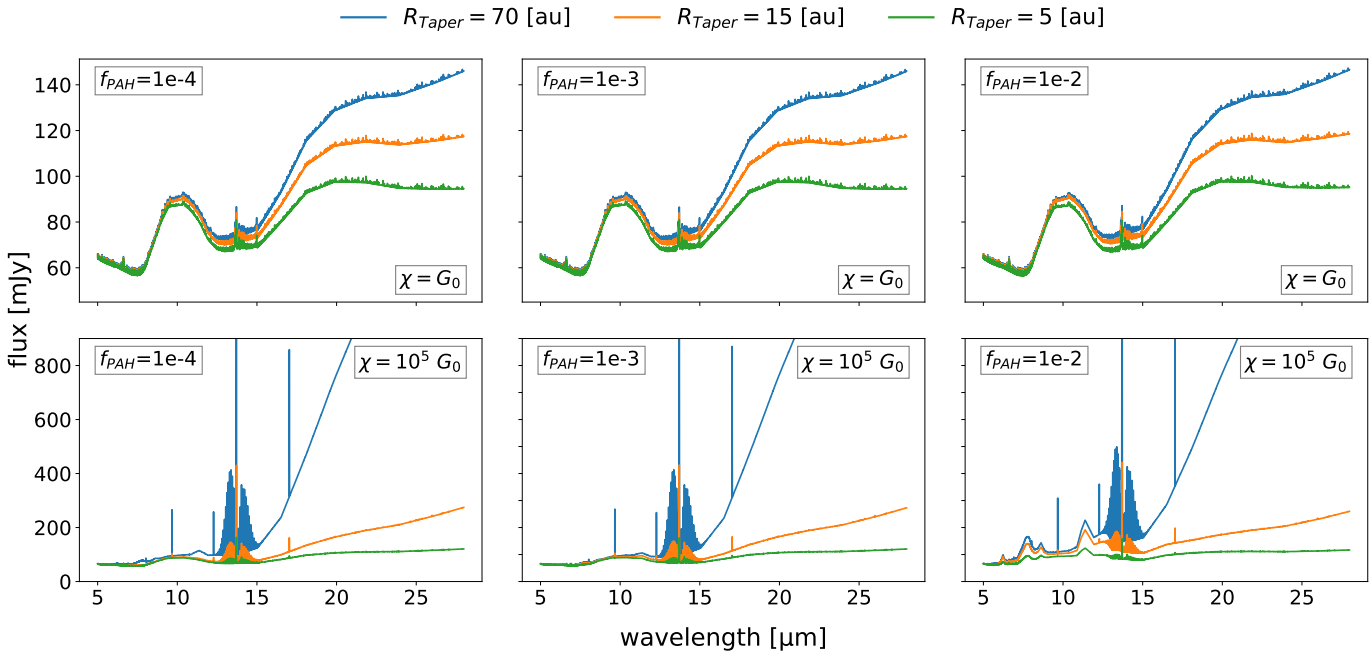

Figure 2. Complete synthetic spectra ranging from 5 to 28 μm. The top row displays models without external irradiation ($\chi = G_0$), while the bottom row illustrates models with extreme external irradiation ($\chi = 10^5 G_0$). Each column represents different fractions of PAH. The strongest emission lines correspond to molecules HCN and C_2H_2.

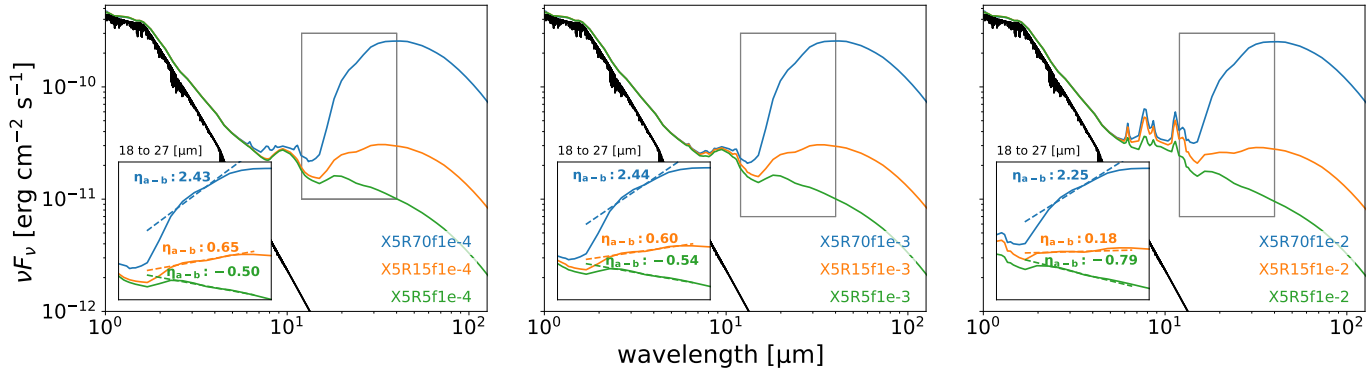

Figure 3. SED for models under extreme external irradiation ($\chi = 10^5 G_0$). The model names are displayed in the lower right corner of each panel. From left to right, the panels correspond to different values of $f_{\rm PAH}$. The boxes in each panel indicate the spectral index calculated between 18 and 27 μm. The black line represents the stellar spectrum.

the disk size modulates the spectral index: larger disks possess more extended dust-emitting areas and thus yield higher spectral indices.

In isolated PPDs, the PAH abundance has no significant effect on the spectral index at a fixed taper radius. In contrast, in irradiated models, increasing PAH abundance leads to a reduction in the spectral index by ∼0.2 for $R_{\rm taper}$ = 70 au, ∼0.4 for 15 au, and ∼0.3 for 5 au (Figure 4). This likely reflects a modest MIR boost from PAH heating and associated emission features. As shown in Figure D2, increased PAH abundance raises the gas temperature primarily in the outer disk regions, boosting the MIR continuum and consequently reducing the spectral index. This effect arises from a pseudocontinuum produced by the superposition of PAH band emission in the MIR, which elevates the continuum at the wavelengths selected to compute the spectral index. As a result, the spectral index becomes sensitive to both the disk truncation and the PAH pseudocontinuum enhancement.

4.1.2. PAH Features

UV radiation also excites PAH molecules to higher electronic states, which then decay to lower electronic states through internal conversion. This process is followed by vibrational and bending vibrational relaxation and de-excitation at wavelengths of 6.2, 7.7, 8.6, 11.2, 12.8, and 16.4 μm (V. C. Geers et al. 2006; R. Chown et al. 2024). In our model series, PAH features appear under an external irradiation field ($\chi = 10^5\ G_0$) and are amplified for higher PAH abundances ($f_{\rm PAH} = 10^{-2}$) and larger disks ($R_{\rm taper}$ = 70 au). Figure 5 shows the normalized local continuum spectra for each PAH feature in the 5–15 μm range, to enhance feature visibility. The figure demonstrates that a strong UV field is essential for detecting PAH features, in agreement with B. Acke et al. (2004). As noted above, increasing the PAH abundance and disk size strengthens the PAH features, reflecting the combined effects of a larger emitting area and a higher PAH abundance.

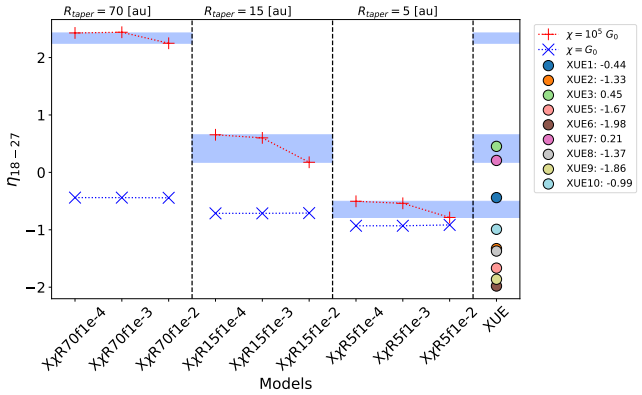

Figure 4. Comparison of the 18–27 μm spectral index across all analyzed models. Colored points show the computed spectral index for the XUE sample (M. C. Ramírez-Tannus et al. 2025). The objects XUE 4, XUE 11, and XUE 12 are not included in the figure because their spectral indices are very small (−3.3, −5.4, and −9.8, respectively). The horizontal blue stripes indicate the range of spectral indices for each $R_{\rm taper}$ in the highly irradiated models.

For models with extreme external irradiation ($\chi = 10^5\,G_0$) and high PAH abundance ($f_{\rm PAH} = 10^{-2}$), the 7.7 and 11.2 μm PAH features are particularly prominent (Figure 5), with fluxes of ∼60 mJy for $R_{\rm taper} = 70$ au and nearly 20 mJy for smaller disks. When $f_{\rm PAH} = 10^{-4}$, the flux drops to ∼5 mJy for both features at $R_{\rm taper} = 70$ au and becomes undetectable for disks with $R_{\rm taper} \leqslant 15$ au. By contrast, in the isolated models, there is no evidence of PAH features, since all fluxes remain below 1 mJy.

As part of the Spitzer Legacy program "From Molecular Cores to Planet-Forming Disks," V. C. Geers et al. (2006) reported that nearly all disks in their sample—comprising three T Tauri stars and five Herbig Ae/Be stars—exhibited robust detections of the 11.2 μm PAH feature. For the T Tauri stars the measured fluxes ranged from 3.3×10^{-16} to 4.0×10^{-15} W m^{-2}, whereas for the Herbig Ae/Be stars the fluxes ranged from 1.2×10^{-15} to 1.4×10^{-14} W m^{-2}.

To quantify the effect of our parameter space on the emission of PAH features and compare with the V. C. Geers et al. (2006) results, we computed the integrated flux of each PAH band. Specifically, we fit a second-order polynomial to the local continuum surrounding each feature and subtract it to isolate the PAH emission. We then integrate the continuum-subtracted spectrum within a ±0.4 μm window centered on each PAH feature to obtain the integrated flux. Table 5 summarizes the integrated fluxes of the 11.2 μm PAH feature (in W m^{-2}) for all models considered in this work, and Figure 6 displays the 11.2 μm feature after the continuum subtraction described above for the integrated flux calculation. The figure compares the most extreme cases (larger disks and higher PAH abundances) and clearly demonstrates how $f_{\rm PAH}$ and $R_{\rm taper}$ regulate the strength of the 11.2 μm emission in externally irradiated models. Overall, our 11.2 μm PAH fluxes are of the same order of magnitude as those reported for Herbig Ae/Be and T Tauri sources (V. C. Geers et al. 2006; C. Joblin & A. G. G. M. Tielens 2020).

Another piece of observational evidence for the presence of PAH features in irradiated PPDs was presented by S. Vicente et al. (2013). They reported integrated fluxes of 29.4 ± 12.9 mJy ((7.8 ± 3.4) × 10^{-15} W m^{-2}) for the 11.2 μm feature in HST10, a proplyd located in a region with an external irradiation field of approximately $\chi \approx 10^5\,G_0$ (H. Störzer & D. Hollenbach 1999). This finding is consistent with our results for the models that involve external irradiation (Table 5).

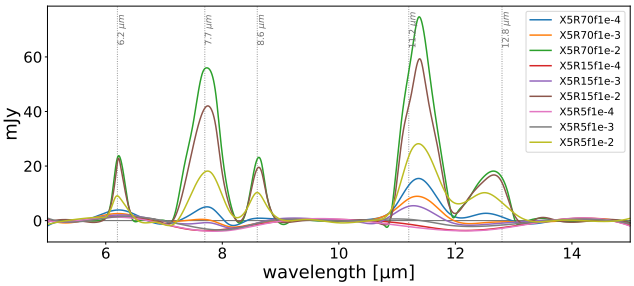

Figure 5. PAH features for externally irradiated models in the 5–15 μm range. Each color corresponds to a different model (Table 3) within the series.

Table 5
Integrated Fluxes in W m^{-2} for the 11.2 μm PAH Feature

Model	Band Flux (W m^{-2})	
	$\chi = G_0$	$\chi = 10^5 G_0$
XχR70f1e-4	1.3×10^{-16}	1.1×10^{-15}
XχR70f1e-3	1.3×10^{-16}	7.8×10^{-16}
XχR70f1e-2	1.6×10^{-16}	5.7×10^{-15}
XχR15f1e-4	1.2×10^{-16}	2.0×10^{-16}
XχR15f1e-3	1.2×10^{-16}	6.2×10^{-16}
XχR15f1e-2	1.3×10^{-16}	4.6×10^{-15}
XχR5f1e-4	1.1×10^{-16}	1.2×10^{-16}
XχR5f1e-3	1.1×10^{-16}	3.5×10^{-16}
XχR5f1e-2	1.1×10^{-16}	1.9×10^{-15}

4.2. Line Emission Analysis

In this subsection, we present the synthetic spectra along with the integrated flux and emission regions for HCN and C_2H_2. We generated the continuum-subtracted synthetic spectra for each species in the range of the MIRI-MRS instrument and calculated the integrated flux (Section 3.3). The continuum subtraction allows us to avoid the effect of the continuum emission on the line strength of the selected species. This way, we can quantify the influence of the outer radius and the PAH abundance on the integrated flux for each molecule in this study.

Since CO_2, H_2O (including both ortho and para forms), and CO are not significantly impacted by either the PAH abundance or the taper radius, we do not include their synthetic spectra or emission regions here. The calculated reduction in integrated flux between models is nearly 10% or less for these molecules (see Figure 7). The emission regions of all these molecules are restricted to the inner part of the disk (less than 10 au), which is consistent with the work of S. Antonellini et al. (2015) and M. Zannese et al. (2024), which shows that in highly irradiated environments water is destroyed by photodissociation, making the emitting region less extended and decreasing the emission strength of the line.

4.2.1. HCN

Here we focus on the HCN feature between 11 and 18 μm, with a specific emphasis on the Q-branch between 13.7 and 14.1 μm (S. Bruderer et al. 2015). To that end, we have generated synthetic spectra covering the 11.9–16.5 μm region,

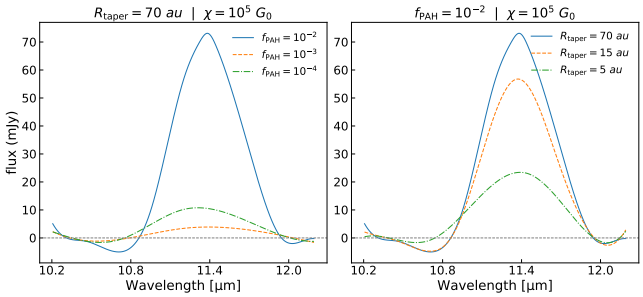

Figure 6. Normalized local continuum for the 11.2 μm PAH feature, illustrating how disk size at fixed PAH abundance (R_{taper}; right panel) and PAH abundance at fixed truncation radius (f_{PAH}; left panel) affect the PAH feature emission for externally irradiated models.

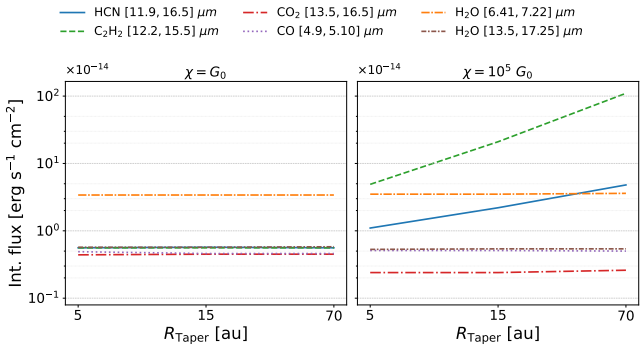

Figure 7. Integrated flux for each species. The integrated flux range for each molecule is indicated in the top legend. The left panel represents isolated PPDs ($\chi = G_0$), while the right panel indicates externally irradiated models ($\chi = 10^5$ G_0). Models with $f_{PAH} = 10^{-2}$ are presented.

shown in Figure 8. As we can see from the figure, there are no discernible effects in the isolated models ($\chi = G_0$) when varying f_{PAH} or R_{taper}. However, it is noteworthy that the truncation radius has a pronounced influence on highly irradiated disks, resulting in a maximum 77% reduction in the integrated flux between models with tapering radii of 70 and 5 au.

Regarding the fractions of PAH at fixed truncation radius, the integrated flux increases by 4% for disks with a taper radius of 70 au when the f_{PAH} is increased from 10^{-4} to 10^{-2}; meanwhile, for disks with a taper radius of 5 au, the flux decreases by nearly 11%. The different behaviors exhibited by models with and without external irradiation can be attributed to the emission region of the HCN molecule. Figure 9 illustrates the emission area for the HCN molecule at 14 μm (Q-branch). In isolated disks the molecule emits from the inner part of the disk's surface, while in highly externally irradiated models the bulk of the emission comes from the outer part of the disk. As shown in Appendix D, the gas temperature structure accounts for this behavior. In isolated models, HCN attains its excitation temperature primarily from central object irradiation, leading to emission concentrated in the inner disk. By contrast, in strongly externally irradiated disks, the HCN emission originates within the warm gas structure described in Appendix D. In this region, the gas temperature reaches ~400 K, which enhances the HCN line emission. Additionally, the dust temperature ranges between 100 and 200 K for all models, enhancing infrared pumping and thereby contributing to the measured fluxes. This effect produces substantial flux differences across models with different truncation radii, given the corresponding reduction in the emitting area with decreasing radius. A non-LTE treatment could explain the low emission of this molecule in the XUE sample, as we can see in Sections 5.2 and 5.3.

4.2.2. C_2H_2

In our analysis of C_2H_2, we focused on the wavelength range between 12.2 and 15.5 μm (Q-branch), as reported in multiple observational data (C. Salyk et al. 2011; I. Pascucci et al. 2013; M. C. Ramírez-Tannus et al. 2023; T. Henning et al. 2024; J. Kanwar et al. 2024). Similarly to HCN, the effect of f_{PAH} over the C_2H_2 flux is negligible for both series of models, with the exception of the largest disk ($R_{taper} = 70$ au) and externally irradiated models, where the integrated flux increases by 9% when the f_{PAH} is increased from 10^{-4} to 10^{-2}. We observe that the flux strongly depends on the truncation radius in highly externally irradiated models. Our findings suggest that there can be a difference of approximately one order of magnitude between each truncation radius, with nearly two orders of magnitude between models with 70 au of taper radius and 5 au, as shown in Figure 10.

Regarding the emission region, upon analyzing Figure 11, we can extend the same line of reasoning as the HCN analysis from the preceding section. For models subjected to an external UV flux of 10^5 G_0, the emitting region depends sensitively on the truncation radius. In these cases, the emission extends nearly the entire disk surface, with gas temperatures exceeding 300 K and dust temperatures of ~200 K in the emitting layers (Appendices D and C, respectively). In externally irradiated models, a notable case arises for models with $R_{taper} = 5$ au, where the emitting region is confined to the inner disk and lies predominantly below the $\tau = 1$ extinction surface at $\lambda = 13.6$ μm. This configuration explains the two-order-of-magnitude reduction in the integrated flux, as well as the potential nondetection of this molecule in such compact disks. The confinement of the emission to the inner regions is primarily a disk size effect: because the disk is less extended, the particle density (e.g., $n_{C_2H_2}$) decreases by roughly two orders of magnitude when evaluated over the same emitting area used for $R_{taper} = 15$ au models. Consequently, about 50% of the total emission originates from the inner disk (Figure 11). By contrast, in isolated models, the emission is also restricted to the inner disk, but in this case due to heating dominated by the central star.

4.3. Line-to-continuum Ratio

To illustrate how MIR gas diagnostics can help determine the truncation state and resolve the degeneracy associated with varying PAH abundances, we present in Figure 12 the ratio of integrated line flux to continuum for each molecule (H_2O, HCN, CO_2, CO, and C_2H_2) across all models. For clarity and comparison, each ratio is normalized to the maximum value obtained for each molecule.

Figure 12 illustrates how the disk size (R_{taper}), PAH abundance (f_{PAH}), and external irradiation field (χ) affect the emission strength of these molecules. In the case of externally irradiated PPDs, disks with R_{taper} of 70 au display greater ratios, with a decrease of nearly 65% for HCN and 90% for C_2H_2 for models with R_{taper} of 5 au. Additionally,

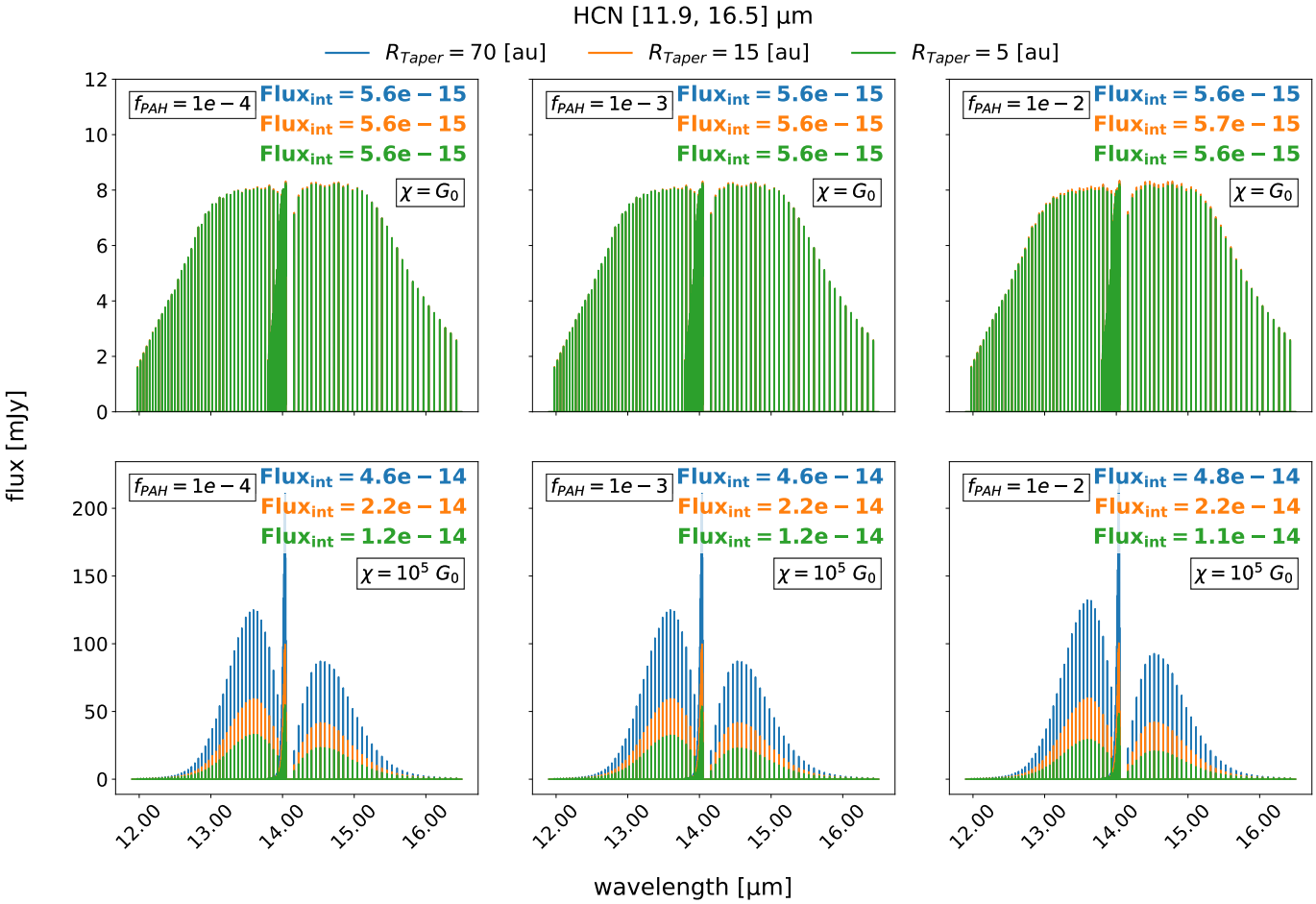

Figure 8. Synthetic spectra of HCN in the 11.9–16.5 μm wavelength range are shown. The top row displays models without external irradiation ($\chi = G_0$), while the bottom row presents models with strong external irradiation ($\chi = 10^5\ G_0$). Colors indicate different truncation radii, and columns correspond to varying PAH abundances. $Flux_{int}$ denotes the integrated line flux (in erg s^{-1} cm^{-2}) for each truncation radius. For isolated disks, the blue and orange curves are overlaid by the green curve because their fluxes are nearly identical.

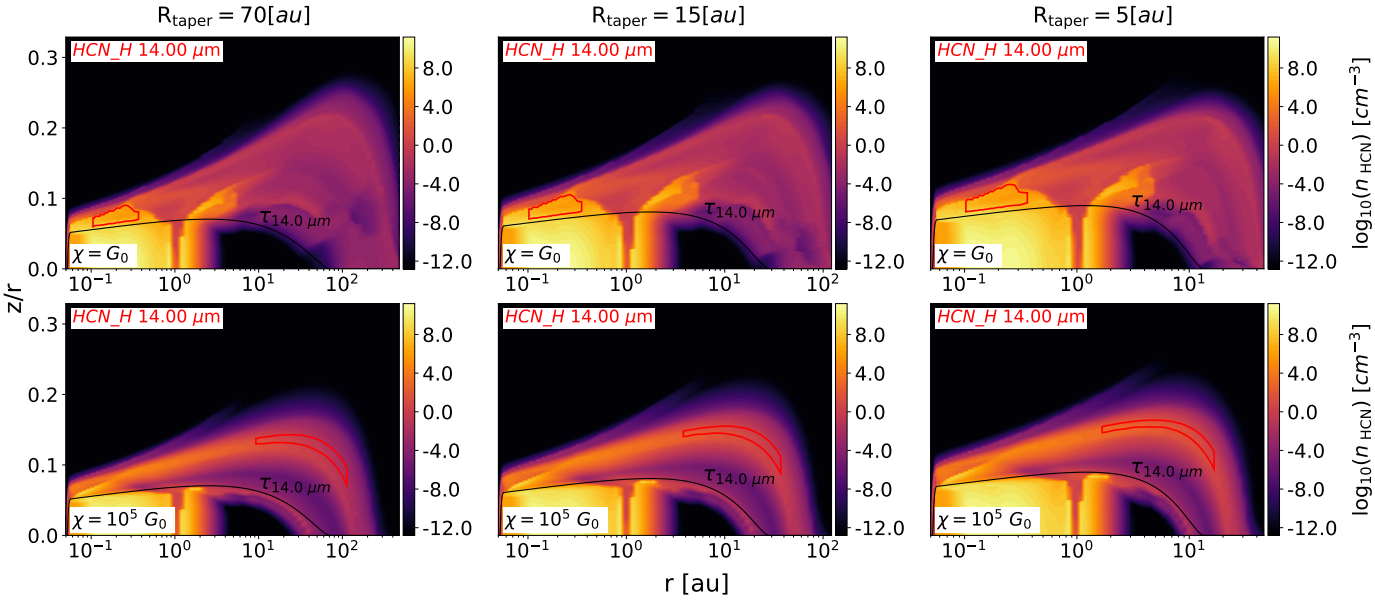

Figure 9. Emission region of HCN for $f_{PAH} = 10^{-4}$. Red boxes indicate the region containing approximately 50% of the total emission, defined by grid points (r, z) where the HCN emission at 14 μm is between 15% and 85% of the local total emission. The black line marks the $\tau_{cont} = 1$ surface at 14 μm. Top row: models without external irradiation. Bottom row: models with extreme external irradiation. The emission area shows no significant dependence on the f_{PAH} parameter for this molecule. The mean of the total vertical column density (N_{HCN}) within the reported emission region is $\sim 10^{21}$ cm^{-2} for isolated models and $\sim 10^{14}$ cm^{-2} for highly externally irradiated models. However, the emission area of the externally irradiated models is $\sim 10^5$ times larger than that of the isolated models, resulting in a flux approximately 10 times stronger for the irradiated models.

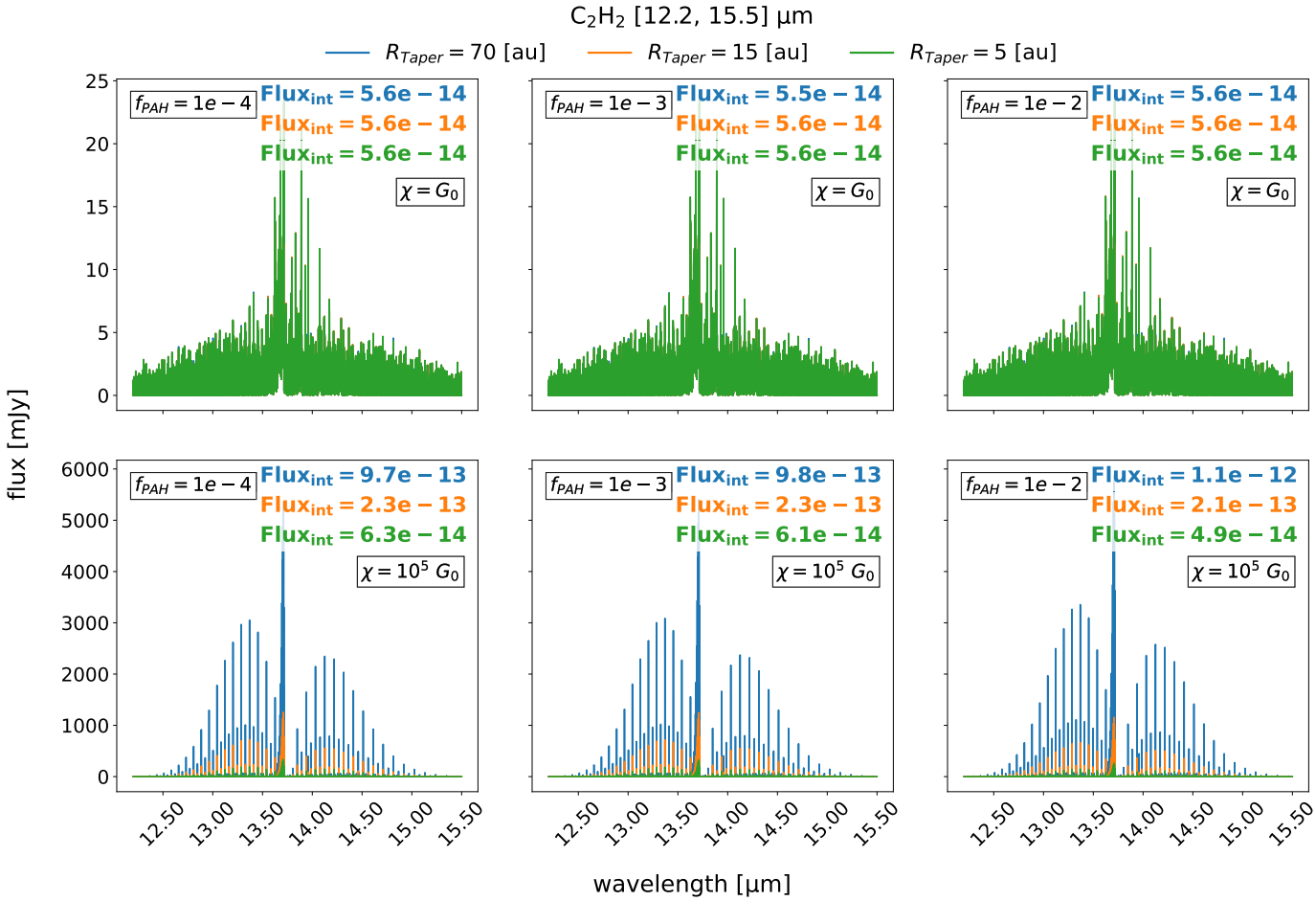

Figure 10. Synthetic spectra of C_2H_2 in the wavelength range of 12.2–15.5 μm are presented. The top row represents models without external irradiation ($\chi = G_0$), while the bottom row illustrates models with extreme external irradiation ($\chi = 10^5\ G_0$). Colors indicate different truncation radii, and columns correspond to varying PAH abundance. $Flux_{int}$ denotes the integrated line flux (in erg s^{-1} cm^{-2}) for each truncation radius. For isolated disks, the blue and orange curves are indistinguishable from the green curve because their fluxes are nearly identical.

the f_{PAH} parameter has a more pronounced effect for $\chi = 10^5 G_0$ and $R_{taper} = 70$ au, as smaller fractions of PAH result in higher line-to-continuum ratios. This is demonstrated by a decrease of almost 20% in the ratio from PAH abundance 10^{-4} to 10^{-2} for both species. Meanwhile, for isolated PPDs, these two species show minimal dependence on R_{taper} and f_{PAH}, showing a greater ratio in small disks and a decrease of approximately 8% between R_{taper} of 5 and 70 au. The f_{PAH} parameter does not affect the line-to-continuum ratio in this scenario.

H_2O and CO_2 show similar trends in both sets of models. In the externally irradiated models, the highest line-to-continuum ratios occur with small disk sizes ($R_{taper} = 5$ au) and low PAH abundance ($f_{PAH} = 10^{-4}$). As the disk size increases to 70 au, the ratio drops by about 30% (in the 6.41–7.22 μm range) and 75% (in the 13.5–17.25 μm range) for H_2O. For CO_2, the decrease is nearly 60%. Increasing the PAH abundance to 10^{-2} further reduces the flux-to-continuum ratio by about 10%. In the isolated models, changes in disk size or PAH abundance have little effect on the flux-to-continuum ratio. The flux-to-continuum ratio for CO remains nearly constant across different truncation radii and PAH abundances. The highest ratio is observed in the smallest disk and at high PAH abundance; however, the difference between different truncation radii is less than 8%, and the PAH abundance does not yield any significant results.

5. Discussion

In this study, we investigated the influence of the truncation radius (R_{taper}), PAH abundance (f_{PAH}), and external irradiation field (χ) on the continuum emission, spectral index, and line emissions of various molecular species (including H_2O, HCN, CO_2, CO, and C_2H_2) in PPDs. Our analysis was based on two distinct sets of models: one simulating an isolated environment ($\chi = G_0$) and another representing a highly externally irradiated environment ($\chi = 10^5\ G_0$). The goal of this study was to provide insights into JWST-MIRI MRS observations of PPDs in strongly irradiated environments, such as those targeted by the XUE program (M. C. Ramírez-Tannus et al. 2025).

5.1. Spectral Index as a Tracer of External Irradiation and/or Disk Truncation?

Our results show that strong external irradiation increases the spectral index (η) for larger disks, while for highly truncated disks η is nearly identical in both cases (Section 4.1.1). The parameter f_{PAH} only plays a role in an externally irradiated disk, where at higher PAH abundance the MIR emission increases owing to the PAH heating (Appendix E), thereby decreasing the spectral index.

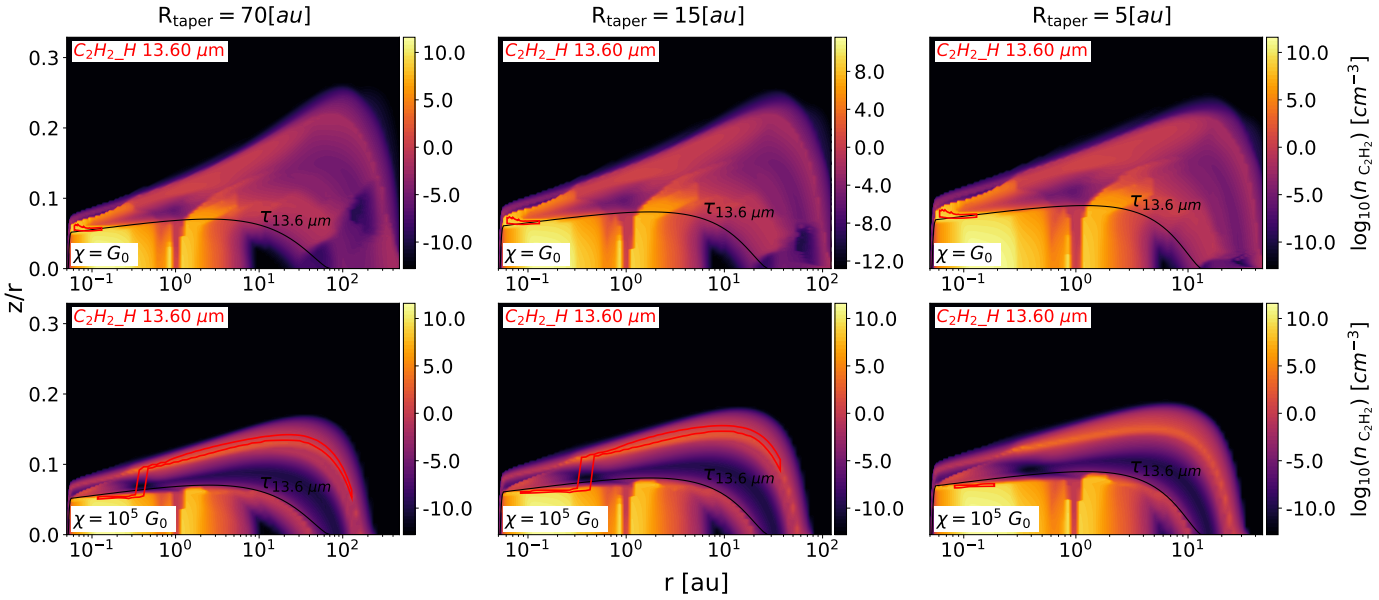

Figure 11. Emission region of C_2H_2 for $f_{PAH} = 10^{-4}$. Red boxes indicate the region containing approximately 50% of the total line emission, defined by grid points (r, z) where the C_2H_2 emission at 13.6 μm is between 15% and 85% of the local total emission. The black line marks the $\tau_{cont} = 1$ surface at 13.6 μm. Top row: models without external irradiation. Bottom row: models with extreme external irradiation. The emission area shows no significant dependence on the f_{PAH} parameter for this molecule. The mean of the total vertical column density ($N_{C_2H_2}$) within the reported emission region is $\sim 10^{19}$ cm^{-2} for isolated models and $\sim 10^{16}$ cm^{-2} for highly externally irradiated models. However, for $R_{Taper} = 70$ and 15 au, the emission area of the externally irradiated models is $\sim 10^5$ times larger than that of the isolated models, resulting in a flux approximately 10 times stronger for the irradiated models. Meanwhile, for $R_{Taper} = 5$ au, both the emission area and the total vertical column density are nearly identical between the two sets of models, yielding a flux of the same order of magnitude.

Our models show a strong dependence of the spectral index on these parameters, indicating its potential as a diagnostic tool. From Figure 4, we see that the spectral index of the XUE 1 source is consistent with a truncated disk, in agreement with observations (M. C. Ramírez-Tannus et al. 2023) and models (B. Portilla-Revelo et al. 2025). For the XUE 10 source (J. Frediani et al. 2025), following the same line of reasoning, the disk must also be truncated to $\leqslant$20 au; however, to explain the abundance of CO_2 in the XUE 10 object, J. Frediani et al. (2025) expose that an inner dust trap or gas cavity between the H_2O and CO_2 ice lines can explain the CO_2-rich spectrum of XUE 10, but requiring that the outer disk is not truncated below $\sim$100 au. An extended disk with substructures, such as cavities, reduces FIR emission and could reproduce both the observed spectral index and the CO_2 abundance, assuming the same disk inclination within our parameter space ($i = 60°$). Additional models exploring disk inclination, truncation radius, and external irradiation (since XUE 10 experiences $\sim 10^3\, G_0$) are therefore required to quantify the spectral index's dependence.

The XUE 1 source demonstrates that, for a fixed disk inclination and external irradiation field, the spectral index in the 18–27 μm range could be a diagnostic of disk size. This spectral index range could thus serve as a disk size indicator: XUE 3 and XUE 7 would be consistent with disk radii of roughly $\sim$150 au, while the remainder of the XUE sample (M. C. Ramírez-Tannus et al. 2025) would be constrained to smaller disks ($\lesssim$50 au). Thus, the spectral index in this wavelength range (18–27 μm) could serve as a first-order estimate of the observable characteristics of PPDs with JWST and other observatories.

5.2. Non-LTE versus LTE Line Emission

We assume here that all emissions are in LTE. However, due to external irradiation, the emission regions of the HCN 14 μm band and the C_2H_2 13.6 μm band extend into the lower-density outer regions of the disk, implying that the line excitation may be subthermal. Although a full non-LTE treatment of these lines is beyond the scope of this work, we estimate the importance of non-LTE effects by employing a two-level approximation for the relative level populations, including dust IR pumping and assuming H_2 as the main collision partner. Our approach is presented in Appendix F.

We use Equation (F6) to calculate the LTE/non-LTE population ratio, $(n_l/n_0)_{LTE}/(n_l/n_0)_{non-LTE}$, assuming T_{rad}, T_{kin}, and n_{H_2} to be the median dust temperature, gas temperature, and number density (in cm^{-3}), respectively, within the emission regions of HCN (Figure 9) and C_2H_2 (Figure 11). If this ratio is close to unity, IR pumping and collisions populate the levels to values close to LTE.

We use typical values for A_{10} and C_{10} (see Appendix F), since A_{ul} and C_{ul} for the molecules C_2H_2 and HCN are unknown. To explore the impact of the dilution factor (w) in Equation (F6), we adopt values of $w = 1$, 0.01, and 0.001. These values are motivated by S. Bruderer et al. (2015), who show that in the inner disks radiation dominates over collisions for $w \gtrsim 10^{-3}$ in the HCN 14 μm band when $T_{rad} = 750$ K and $n_{H_2} = 10^9$ cm^{-3}.

Table 6 presents our results. The dilution factor has a strong impact on HCN, reducing the non-LTE-to-LTE population ratio by about an order of magnitude for highly truncated disks ($R_{taper} = 5$ au). In contrast, for C_2H_2 the impact is negligible in truncated disks. We find that for these disk sizes ($R_{taper} = 5$ au) both molecules (HCN and C_2H_2) exhibit population ratios close to LTE, even when dilution is included. In particular, C_2H_2 remains very close to LTE. This suggests that the truncation radius may influence the line emission strength. In future work, we will perform a full non-LTE treatment of these transitions, with particular emphasis on HCN, which appears to deviate the most from LTE according to our initial estimates.

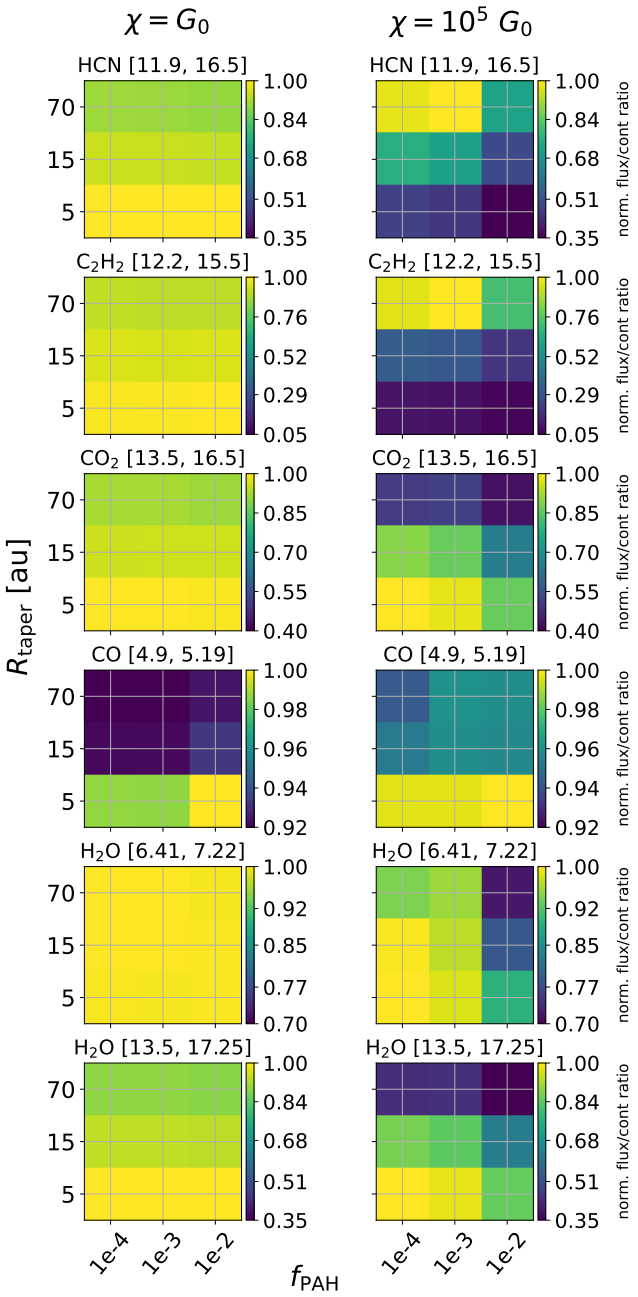

Figure 12. Trend map of the ratio of integrated emission-line flux to integrated continuum flux. For each species, the line emission and continuum fluxes are integrated over the range specified for each molecule. The highest ratio for each molecule is used to normalize the map for that specific molecule.

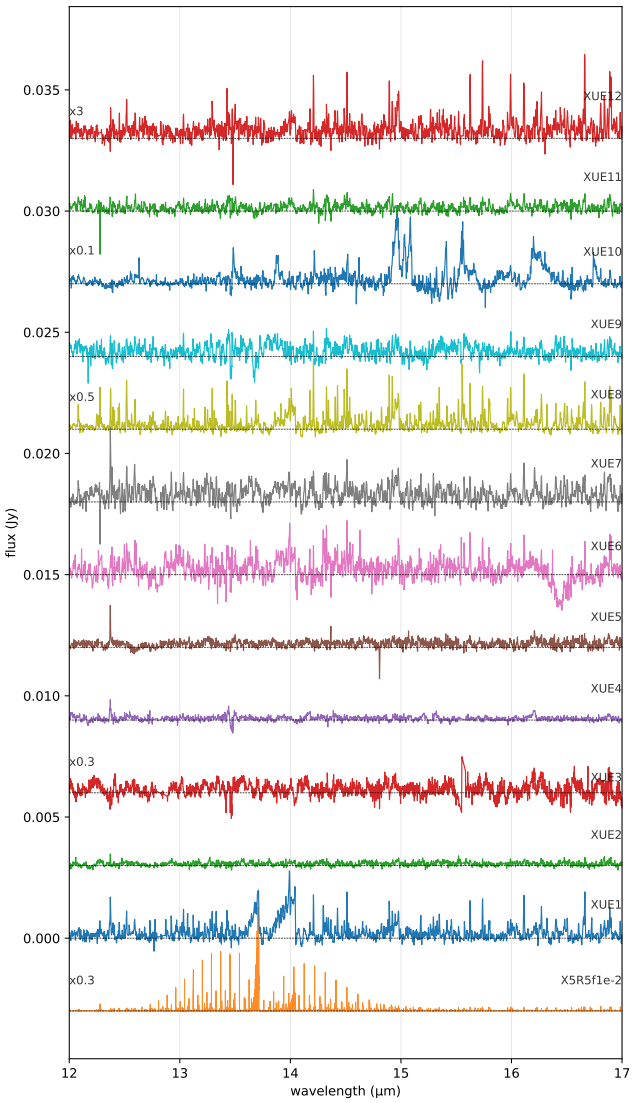

Figure 13. Model X5R5f1e-2 compared with the XUE sample.

5.3. Line Emission Strength

After scaling our results to the distance of the XUE sources, from 400 pc to 1.69 kpc (M. C. Ramírez-Tannus et al. 2025), the line spectral intensities are of the same order of magnitude as those observed in the XUE sample for nearly all species, as shown in Figure 13. As discussed in the previous section, HCN is far from LTE; consequently, our models produce stronger lines in the 13–15 μm range than their observational counterpart (see Figure 13). This suggests that the emission observed in the XUE sample may also arise under non-LTE conditions.

As reported by B. Portilla-Revelo et al. (2025) and M. C. Ramírez-Tannus et al. (2023), the XUE 1 source could be gas depleted beyond 10 au. Because our smallest disk size is nearly 50 au, a smaller truncation radius could account for the reduced line emission of these molecules (C_2H_2 and HCN). Our results demonstrate a strong dependence of the molecular line fluxes on R_{taper} when an external irradiation field is applied. We review in Section 5.2 how the C_2H_2 level populations remain close to LTE across all disk sizes, in particular for the smallest disks, supporting this interpretation. Thus, our models may serve as an initial framework for characterizing the disk size of T Tauri sources in high-mass SFRs.

5.4. Are the XUE Sources Truncated?

B. Portilla-Revelo et al. (2025) reported that a truncated, gas-depleted disk beyond 10 au can reproduce the MIR MIRI/MRS spectrum of XUE 1, assuming external irradiation of $\chi = 10^5\ G_0$ consistent with the estimated flux based on the projected distance to the nearby OB stars in Pismis 24. In their work, they explore different disk sizes while holding the disk mass fixed. In this work, we scale the disk mass with truncation radius while maintaining a constant inner-disk density. Whereas B. Portilla-Revelo et al. (2025) aim to model the specific XUE 1 system, our study models T Tauri disks

Table 6
LTE-to-non-LTE-level Population Ratios, $(n_l/n_0)_{\rm LTE}/(n_l/n_0)_{\rm non-LTE}$, for Externally Irradiated Models and $f_{\rm PAH} = 1e-2$

$R_{\rm taper}$ (au)	$T_{\rm kin}$ (K)	$T_{\rm rad}$ (K)	$n_{\rm H_2}$ (cm^{-3})	$w = 1$	$w = 0.01$	$w = 0.001$
			HCN			
70	363	117	6.9e8	0.009	0.006	0.006
15	359	186	1.6e9	0.083	0.016	0.015
5	372	330	6.2e9	0.721	0.065	0.058
			C_2H_2			
70	317	218	7.0e9	0.269	0.067	0.065
15	319	261	2.6e10	0.582	0.213	0.209
5	552	561	4.5e13	1	0.997	0.997

with stellar parameters matching those of XUE 1. As our results show (spectral index and line emission strength), both approaches are consistent with XUE 1 having a disk truncated at $\sim$10 au.

Consistent with this, M. C. Ramírez-Tannus et al. (2025) report that none of the disks in the XUE sample exhibit extremely strong lines. The present study provides a possible explanation for these observations, suggesting that the lack of strong lines may be a consequence of disk truncation across the sample.

On the other hand, the XUE disks could be shielded from FUV photons, reducing the external irradiation field and the photoevaporation rate and thereby yielding larger disks. M. Gárate et al. (2024) demonstrate that dust grains carried by photoevaporative winds can produce a self-shielding effect, as the dust can attain an FUV absorption cross section of $\sigma \approx 10^{-22}\,{\rm cm}^2$ during the early evolutionary stages (<0.1 Myr). This mechanism could also help explain the spectral characteristics observed by JWST.

However, the extinction hypothesis for the XUE sample appears unlikely, as all disks lack strong lines (J. Frediani et al. 2025; M. C. Ramírez-Tannus et al. 2025). Furthermore, both the models presented by B. Portilla-Revelo et al. (2025) and the results of this study provide strong evidence for disk truncation.

5.5. Dust Temperature Structure

J. K. Calahan et al. (2025) reported that external UV irradiation increases the dust temperature throughout the disk. They also included viscous heating from accretion, which has a significant impact within the innermost au of the disk; nevertheless, these inner regions are not affected by the external irradiation field, since they contain the highest dust and gas densities, leading to substantial attenuation of external UV photons. They reported an increase in dust temperature due to external irradiation in the outer disk, causing some molecular ice lines to bend and intersect the midplane at two locations, one in the inner disk and another in the outer disk, with implications for the chemical evolution of the disk. As we show in Appendix C, our dust temperature structure reproduces the same behavior reported by J. K. Calahan et al. (2025). As they present, heating from accretion affects the innermost regions ($\leqslant$2 au) but does not affect the overall temperature structure.

They also reported that within $\leqslant$1 au and for scale heights $z/r \leqslant 0.15$ the dust temperature structure remains approximately constant (as discussed above), in agreement with our results (Figure C1) for all truncation radii and externally irradiated models. Meanwhile, the outer disk ($\gtrsim$1 au) becomes warmer by several tens of kelvin near the midplane and by a few hundred kelvin at larger scale heights. In both studies, the outer disk (even near the midplane) exhibits higher temperatures toward the disk edge.

Another important point from their findings concerns the impact of disk composition on the observable abundance of key molecules such as HCN and C_2H_2. J. K. Calahan et al. (2025) reported that, for these molecules, the total observable abundance decreases by less than an order of magnitude in externally irradiated environments ($\chi = 10^5\,G_0$), with HCN being more strongly affected. However, if the C/O ratio is sufficiently high (C/O = 2), the observable abundance of both molecules increases by less than an order of magnitude. This may also help explain the lack of strong C_2H_2 and HCN line emission in some XUE sources (M. C. Ramírez-Tannus et al. 2025). Nevertheless, the dependence of line emission strength on truncation radius presented in this work, together with the XUE 1 models of B. Portilla-Revelo et al. (2025), suggests that truncation radius has a larger impact on line emission strength than the disk's chemical composition, since the abundance reductions for these two molecules are less than an order of magnitude (J. K. Calahan et al. 2025).

6. Conclusions

We presented how disk truncation ($R_{\rm taper}$), the abundance of PAH ($f_{\rm PAH}$), and the external irradiation field (χ) impact the spectral characteristics of PPDs. Our goal is to help characterize the structure of the PPDs in the XUE sample (M. C. Ramírez-Tannus et al. 2025). In the following, we summarize the main findings of this study.

1. The disk size ($R_{\rm taper}$) has a major impact on the spectral characteristics of PPDs, affecting both the spectral index analyzed (Section 4.1.1) and the line emission strength (Sections 4.2 and 4.3). Thus, the XUE sample must be truncated to the first tens of astronomical units. Only XUE 3 and XUE 7 could have disk sizes of $\sim$150 au, according to the spectral index analysis (Section 5.1).
2. The detectability and emission strength of PAH features in PPDs depend critically on the intensity of external UV irradiation, as well as on disk size and PAH abundance. A sufficiently strong UV field ($\gtrsim 10^3\,G_0$) is required for PAH features to stand out (J. Frediani et al. 2025). In our externally irradiated models, the 11.2 μm PAH feature emerges as the most reliable tracer of PAH abundance, as it appears across all disk sizes when an external UV field is applied. However, the PAH emission strength depends strongly on disk size ($R_{\rm taper}$) and PAH abundance ($f_{\rm PAH}$): if the disk is highly truncated ($R_{\rm taper} \leqslant 5$ au) and $f_{\rm PAH} \leqslant 10^{-3}$, the 11.2 μm feature may remain undetected, which could explain the lack of PAH features in the XUE sample (M. C. Ramírez-Tannus et al. 2025).
3. The $f_{\rm PAH}$ parameter does not influence the emission area for any of the molecular species considered: even when comparing models with PAH abundances that differ by two orders of magnitude, the relative differences in

emission area remain below 1%, which could be explained by the thermal structure (see Appendices C and D). In contrast, the line emission is more sensitive to both the disk truncation radius ($R_{\rm taper}$) and, to a lesser extent, $f_{\rm PAH}$ in externally irradiated disks. The HCN and C_2H_2 lines are particularly sensitive to changes in $R_{\rm taper}$: for smaller disks, both the integrated flux (Section 4.2) and the line-to-continuum ratio (Section 4.3) decrease significantly—by about 65% for HCN and 90% for C_2H_2. Additionally, variations in $f_{\rm PAH}$ by a factor of 100 can still induce changes of up to 20% in the emission of these molecules in externally irradiated models.

4. The absence of strong C_2H_2 line emission in the XUE sample (M. C. Ramírez-Tannus et al. 2025) supports the truncation hypothesis across all sources. This is consistent with the molecule's strong dependence on disk size in highly irradiated environments ($\sim 10^5 G_0$), where smaller disks exhibit significantly weaker line emission (as demonstrated in Section 4.2.2). Consequently, both observations and models of highly irradiated PPDs suggest that disk truncation is the most plausible scenario.

Overall, our simulations provide valuable context for interpreting observations from the MIRI-MRS instrument on JWST and other observatories. They demonstrate how disk size and PAH abundance shape the spectral index and line fluxes of PPDs in massive SFRs.

Acknowledgments

M.C.R-T. acknowledges support by the German Aerospace Center (DLR) and the Federal Ministry for Economic Affairs and Energy (BMWi) through program 50OR2314 "Physics and Chemistry of Planet-forming disks in extreme environments." E.S. is supported by the international Gemini Observatory, a program of NSF NOIRLab, which is managed by the Association of Universities for Research in Astronomy (AURA) under a cooperative agreement with the US National Science Foundation, on behalf of the Gemini partnership of Argentina, Brazil, Canada, Chile, the Republic of Korea, and the United States of America. V.R. acknowledges the support of the European Union's Horizon 2020 research and innovation program and the European Research Council via the ERC Synergy Grant "ECOGAL" (project ID 855130). A.J.W. has received funding from the European Union's Horizon 2020 research and innovation program under the Marie Sklodowska-Curie grant agreement No. 101104656 and the Royal Society's University Research Fellowship. T.J.H. acknowledges UKRI guaranteed funding for a Horizon Europe ERC consolidator grant (EP/Y024710/1) and a Royal Society Dorothy Hodgkin Fellowship. A.B. and J.F. acknowledge support from the Swedish National Space Agency (grant No. 2022-00154). The FACom group is supported by Convocatoria Programática 2023-2024—Ciencias Exactas y Naturales, Universidad de Antioquia, Project: 2024-76923, CODI 926.

Appendix A
Gas Density Contour Map

Figure A1 plots de gas density contour map for externally irradiated models. Since we utilized a parameterized model, the gas density distribution remains consistent across various values of PAH. Meanwhile for the different truncation radii, the inner disk density remains the same.

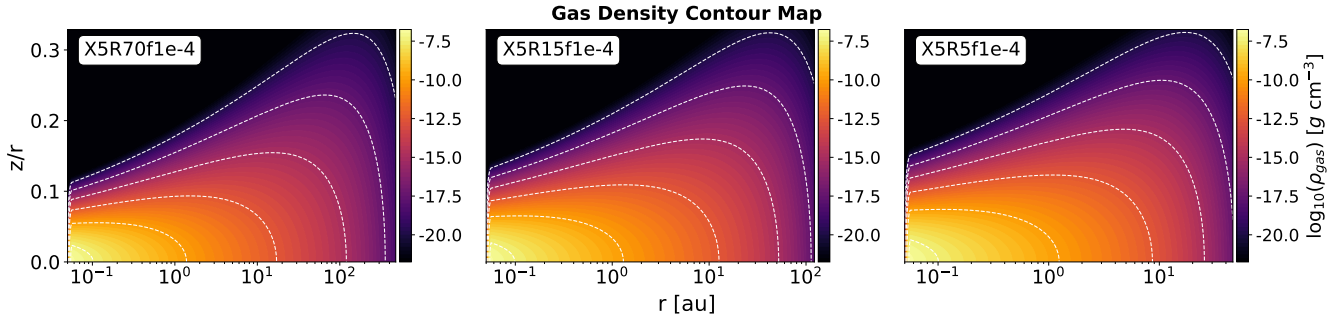

Figure A1. Gas density contour map (in g cm^{-3}), presenting the externally irradiated models ($\chi = 10^5\ G_0$). Each panel corresponds to a different value of $R_{\rm taper}$. The text in each panel refers to the model names as indicated in Table 3.

Appendix B
SED for Isolated PPDs ($\chi = G_0$)

Figure B1 plots the SED for isolated models. In this escenario the PAH abundance parameter does not affect the spectral index; however, the truncation parameter does.

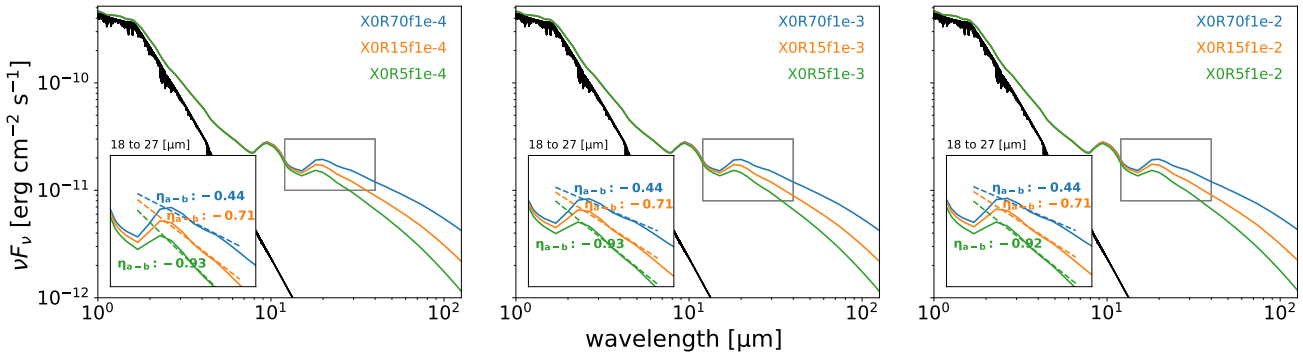

Figure B1. SED for isolated models ($\chi = G_0$). The model names are displayed in the upper right corner of each panel (Table 3). From left to right, the panels correspond to different values of $f_{\rm PAH}$, and each panel presents different disk sizes ($R_{\rm taper}$). The boxes in each panel indicate the spectral index calculated between 18 and 27 μm. The black line represents the stellar spectrum.

Appendix C
Dust Temperature Contour Map

The following dust temperature contour maps illustrate the impact of the external irradiation field. In models without external irradiation, heating is dominated by the central star. Consequently, the outer disk remains relatively cool: the coldest regions (30 K or below) lie near the midplane ($z/r < 0.1$), while the disk surface is moderately warmer, with temperatures between 80 and 200 K. This behavior is illustrated in the top row of Figure C1.

In externally irradiated models, heating is driven by both the central star and the external irradiation field. Consequently, the outer disk becomes warmer, with the 80–200 K region extending outward and approaching the midplane. The coldest dust (<45 K) remains confined to the midplane at radii near 10 au from the central star, leaving the outer disk comparatively warm. While the outer optically thin part of the disk is efficiently heated, UV photons cannot penetrate into the central regions, resulting in the observed thermal structure (bottom row of Figure C1). The parameters $R_{\rm taper}$ and $f_{\rm PAH}$ have no major impact on the dust temperature distribution.

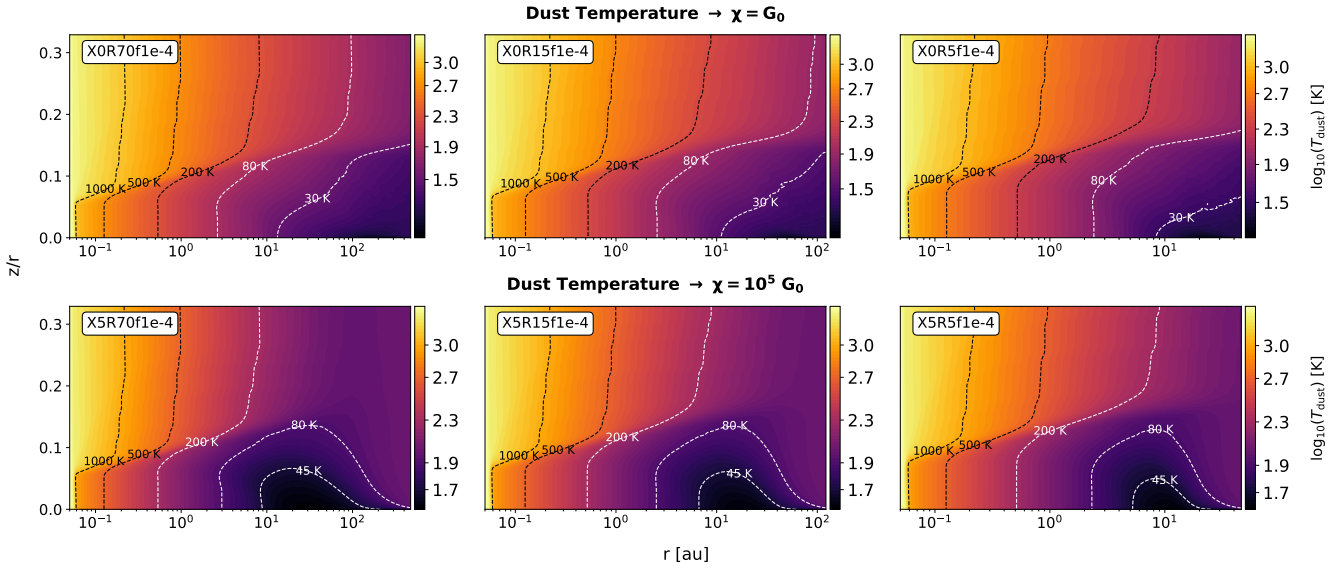

Figure C1. Dust temperature contour map (in K). The top row shows isolated PPDs models ($\chi = G_0$), while the bottom row presents externally irradiated models ($\chi = 10^5 G_0$). Each column corresponds to a different value of $R_{\rm taper}$. Model names are indicated in the upper left corner of each panel (see Table 3). Since $f_{\rm PAH}$ does not affect the dust temperature, we only display the case with $f_{\rm PAH} = 1e-4$.

Appendix D
Gas Temperature Contour Map

The external irradiation field has a major impact on the gas temperature structure. Figures D1 and D2 present gas temperature contour maps for isolated PPDs and externally irradiated disks, respectively. In isolated models ($\chi = G_0$), the parameters $R_{\rm taper}$ and $f_{\rm PAH}$ have a negligible effect on the gas temperature; it remains nearly unchanged across disk sizes and PAH abundances. This behavior arises because the dominant irradiation source is the central star, combined with the adopted parametric gas density distribution. As a result, the disk surface remains warm (approximately 450 K), whereas the outer disk at deeper layers ($z/r < 0.15$) stays cold, with temperatures below 20 K.

In contrast, for externally irradiated PPDs ($\chi = 10^5\ G_0$), the central star is not the sole irradiation source. External FUV photons heat the gas by roughly 300 K at the disk surface and by several tens of kelvin in deeper layers (near the midplane at $\sim$10 au). The parameter $R_{\rm taper}$ does not noticeably affect the gas temperature distribution, consistent with the adopted parametric gas density profile and mass scaling (Table 3). By contrast, the parameter $f_{\rm PAH}$ plays a significant role. Increasing the PAH abundance from 10^{-4} to 10^{-2} raises the gas temperature in the outer disk by approximately an order of magnitude. This enhancement arises from efficient photoelectric heating: PAH grains absorb FUV photons from nearby O stars and transfer energy to the gas, producing strong PAH-driven heating (see Appendix E).

Another notable feature of the gas temperature distribution in PPDs exposed to an external irradiation field is a warm structure that emerges near $\sim$10 au and at scale heights above $z/r \sim 0.15$, extending downward toward the midplane (Figure D2). This feature attains peak temperatures of approximately 750 K at its center; we neglected the effect of photoevaporation. As shown in Figure E2, the dominant processes in this region are H_2 photon heating and OH rovibrational cooling. The extreme external FUV field provides a natural explanation for this structure: enhanced FUV irradiation dissociates H_2 molecules, depositing energy into the gas. In these extreme environments, this heating mechanism is more efficient than the OH rovibrational cooling, thereby producing the observed temperature enhancement.

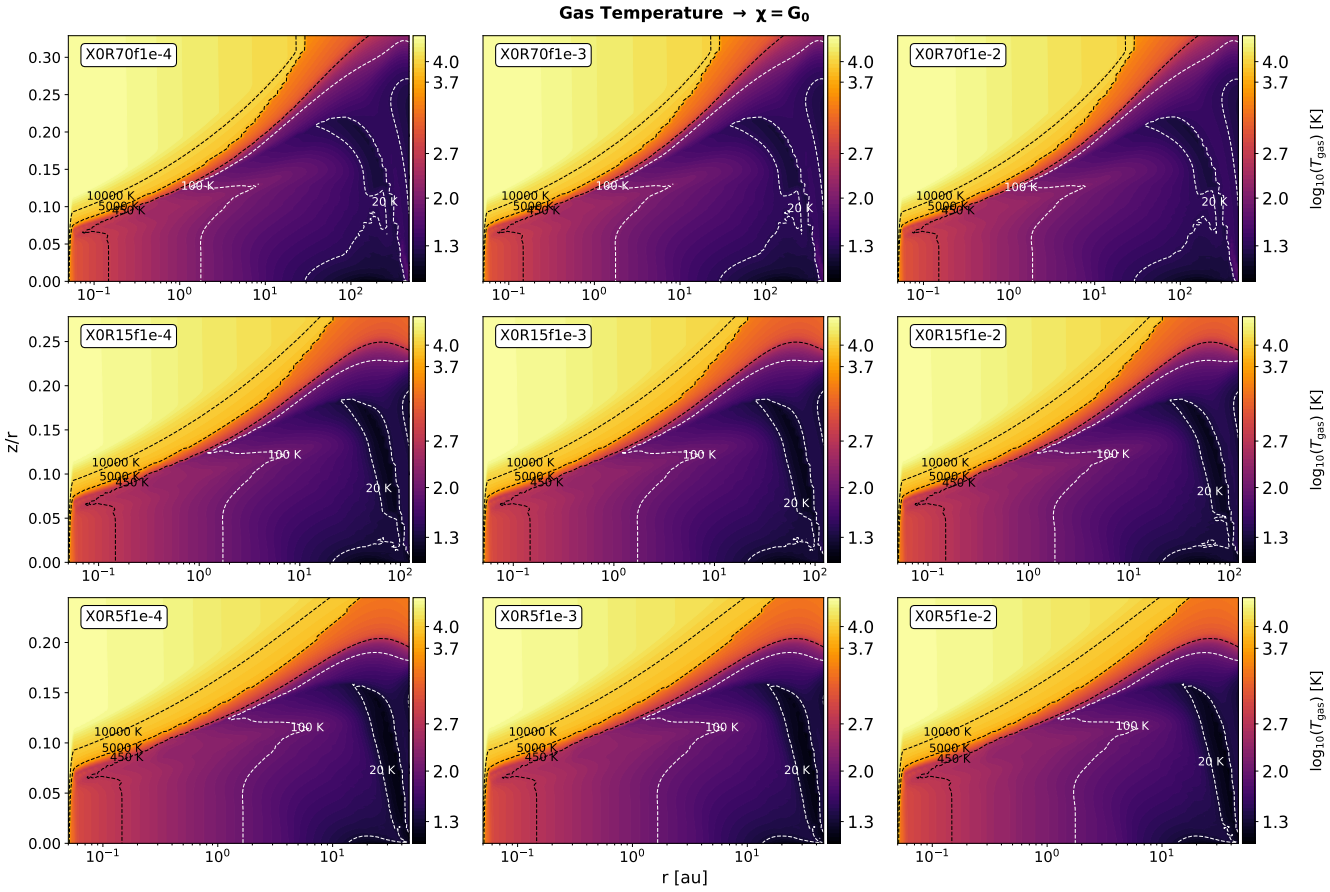

Figure D1. Gas temperature contour map (in K) for isolated PPDs ($\chi = G_0$). Each panel corresponds to different model configurations as detailed in Table 3.

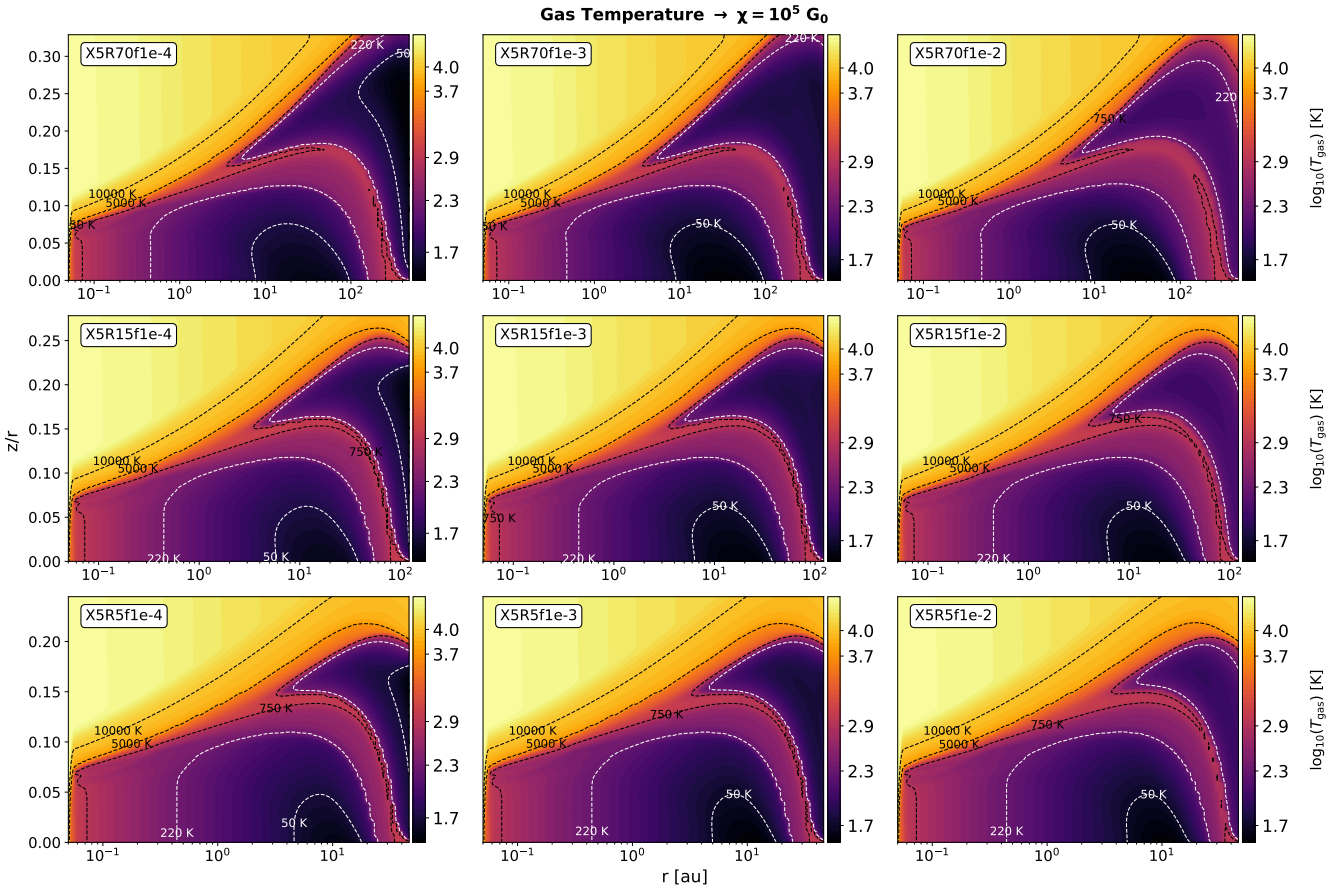

Figure D2. Gas temperature contour map (in K) for externally irradiated PPDs ($\chi = 10^5 G_0$). Each panel represents a distinct model configuration, as outlined in Table 3.

Appendix E
Heating−Cooling Processes

The dominant heating and cooling processes in our model series are shown in Figures E1 ($\chi = G_0$) and E2 ($\chi = 10^5\ G_0$). These figures present the dominant processes for representative models characterized by $R_{\rm taper} = 70$ au and $f_{\rm PAH} = 10^{-2}$. To understand the heating and cooling processes throughout the disk, we focus on 0.5 au to examine the inner disk, 70 au for the mid-disk, and 200 au for the outer disk. The values 70 and 200 au were chosen because they correspond to the largest scale height in the gas thermal structure presented in the previous section (Appendix D), and 200 au lies near the outer edge of the structure. Table 7 lists the most dominant heating/cooling processes at 70 au and their corresponding z/r ranges for both models.

In the inner disk (0.5 au), the dominant heating processes are dust thermal accommodation near the midplane, background heating by CO rovibrational emission at intermediate scale heights, and X-ray Coulomb heating in the upper layers for both sets of models, externally irradiated and isolated. The PAH-heating process appears only in externally irradiated models and at a scale height near $z/r \sim 0.08$. The dominant cooling processes in this region are H_2O, CO, and OH rotational and rovibrational cooling near the midplane ($z/r \leqslant 0.1$), while O III line cooling dominates in the upper layers.

As presented in Table 7, at 70 au and near the midplane ($z/r \leqslant 0.1$), PAH heating dominates in the externally irradiated models, while in the isolated models cosmic-ray heating is the dominant process. At this same scale height, the dominant cooling processes are dust thermal accommodation for the externally irradiated models and OH rotational and H_2O rotational and rovibrational cooling for the isolated models. The PAH-heating process appears only in the externally irradiated models, occurring at two scale heights: first at $z/r \sim 0.11$ and again at $z/r \sim 0.2$. In the upper layers, the dominant heating mechanism is X-ray Coulomb heating, extending to $z/r = 0.23$ in the isolated models and $z/r = 0.3$ in the externally irradiated models.

In the outer part of the disk ($r = 200$ au), near the end of the gas thermal structure (Figure D2), the external irradiation field has a stronger impact. Near the midplane ($z/r \leqslant 0.1$), heating by H_2 de-excitation and OH rovibrational cooling dominate in externally irradiated PPDs, while in isolated models cosmic-ray heating and H_2O rotational and rovibrational cooling dominate. The PAH-heating process also plays a significant role in the externally irradiated models, dominating at scale heights between $z/r = 0.12$ and $z/r = 0.27$, contributing to the development of the thermal structure shown in Figure D2.

In isolated PPDs PAH heating is nearly negligible, whereas in externally irradiated models it becomes more significant. Many cooling processes differ between the isolated and externally irradiated model series. The most representative example is fine-structure line cooling. The O I cooling region

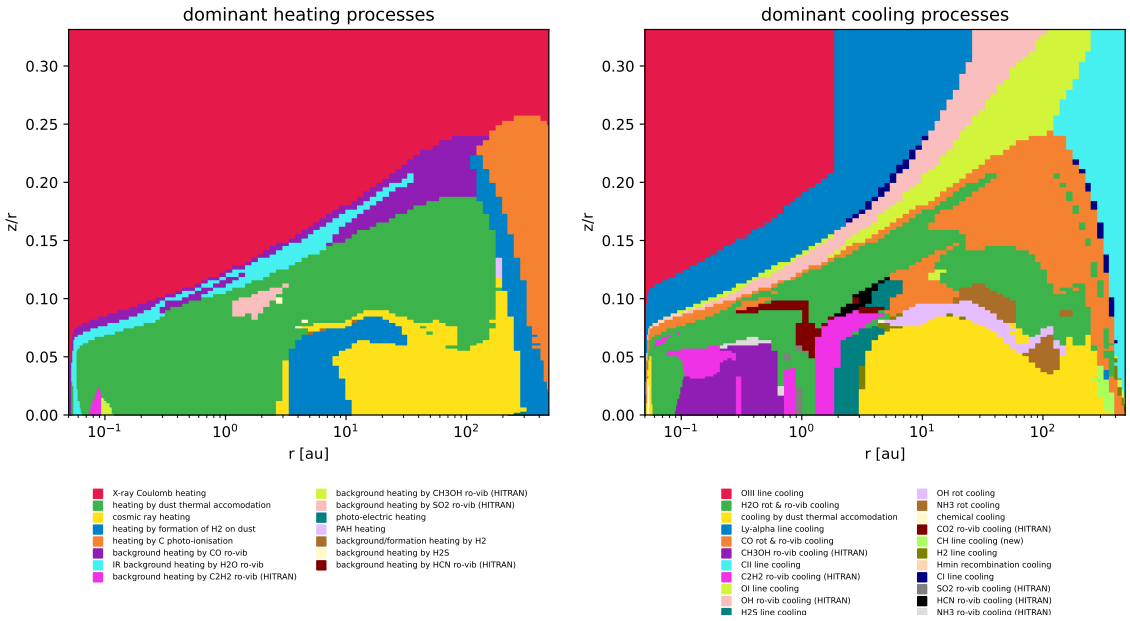

Figure E1. Heating–cooling processes for isolated PPDs ($\chi = G_0$, $R_{\rm taper} = 70$ au). The left panel shows the dominant heating processes, while the right panel shows the dominant cooling processes.

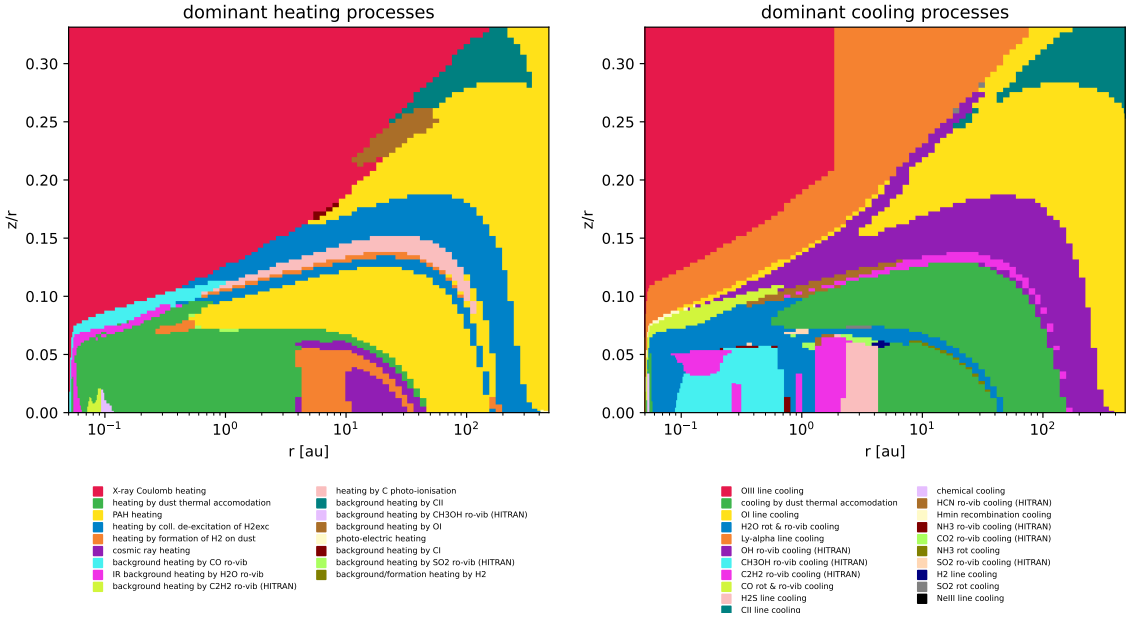

Figure E2. Heating–cooling processes for externally irradiated PPDs ($\chi = 10^5 G_0$, $R_{\rm taper} = 70$ au). The left panel shows the dominant heating processes, while the right panel shows the dominant cooling processes.

expands and penetrates deeper into the disk when an external UV radiation field is applied, while in isolated disks it remains confined to the disk surface. By contrast, the C II cooling region shrinks under external irradiation, whereas in isolated models it extends toward the midplane.

The parameters $R_{\rm taper}$ and $f_{\rm PAH}$ do not play a major role. Increasing the disk size primarily scales certain heating and cooling regions proportionally, and increasing the PAH abundance similarly enlarges the PAH-heating region in the externally irradiated models.

Table 7
Dominant Heating/Cooling Processes as a Function of z/r at $r \simeq$ 70 au for Two Radiation Fields: $\chi = G_0$ and $\chi = 10^5\ G_0$

$\chi = G_0$			$\chi = 10^5\ G_0$		
z / r Range	Heating	Cooling	z / r range	Heating	Cooling
[0.000, 0.050]	cosmic-ray heating	cooling by dust thermal accommodation	[0.000, 0.100]	PAH heating	cooling by dust thermal accommodation
[0.052, 0.052]	cosmic-ray heating	NH3 rot cooling	[0.103, 0.106]	heating by coll. de-excitation of H2exc	OH rovibrational cooling
[0.055, 0.057]	cosmic-ray heating	OH rot cooling	[0.109, 0.112]	heating by coll. de-excitation of H2exc	C_2H_2 rovibrational cooling
[0.059, 0.059]	heating by dust thermal accommodation	OH rot cooling	[0.115, 0.115]	heating by formation of H2 on dust	C_2H_2 rovibrational cooling
[0.061, 0.061]	cosmic-ray heating	OH rot cooling	[0.118, 0.118]	PAH heating	OH rovibrational cooling
[0.064, 0.068]	cosmic-ray heating	cooling by dust thermal accommodation	[0.121, 0.137]	heating by C photo-ionization	OH rovibrational cooling
[0.071, 0.076]	cosmic-ray heating	H2O rot & rovibrational cooling	[0.140, 0.182]	heating by coll. de-excitation of H2exc	OH rovibrational cooling
[0.078, 0.140]	heating by dust thermal accommodation	H2O rot & rovibrational cooling	[0.186, 0.186]	heating by coll. de-excitation of H2exc	OI line cooling
[0.143, 0.186]	heating by dust thermal accommodation	CO rot & rovibrational cooling	[0.190, 0.268]	PAH heating	OI line cooling
[0.190, 0.234]	background heating by CO rovibrational	CO rot & rovibrational cooling	[0.273, 0.277]	background heating by CII	OI line cooling
[0.238, 0.305]	X-ray Coulomb heating	OI line cooling	[0.282, 0.296]	background heating by CII	CII line cooling
[0.310, 0.329]	X-ray Coulomb heating	OH rovibrational cooling	[0.300, 0.319]	X-ray Coulomb heating	OI line cooling
…	…	…	[0.324, 0.329]	X-ray Coulomb heating	Lyα line cooling

Appendix F
IR LTE versus Non-LTE Population Ratios

To assess how the LTE assumption impacts the results of this work—given that the emission regions of C_2H_2 and HCN in externally irradiated models lie in the low gas density regime of the PPD—we perform an order-of-magnitude estimate to compare LTE and non-LTE population ratios.

First, we derive the IR pumping level population, taking into account that the ratio between the first excited vibrational level and the ground state for a gas in a radiation field of temperature $T_{\rm rad} = T_{\rm dust}$, expressed in terms of the wavenumber $\tilde{\nu}$ (in cm^{-1}), is given by

$$\frac{n_1}{n_0} = \frac{g_1}{g_0} \frac{1}{\exp\left(\frac{1.44\,\tilde{\nu}}{T_{\rm rad}}\right) - 1}, \tag{F1}$$

where the factor 1.44 converts cm^{-1} to K ($hc/k = 1.44$ cm K). From this expression, we can derive the dust temperature required to maintain significant excitation of a molecule's vibrational levels. For example, considering excitation of the ν_3 vibrational mode of C_2H_2, the C≡C stretching mode ($\tilde{\nu} = 818$ cm^{-1}, $\nu = 12.2\ \mu$m), and assuming $g_1/g_0 = 1$, for a given population ratio $n_1/n_0 = 10^{-3}$ and solving for the radiation field temperature, we obtain

$$T_{\rm rad} = \frac{1.44 \times 818}{\ln(1 + 10^3)} \approx \frac{1178}{6.9} \approx 171\ {\rm K}. \tag{F2}$$

An IR field with $T_{\rm rad} \gtrsim 170$ K is therefore sufficient to maintain a significant excitation ($n_1/n_0 \sim 10^{-3}$) of the vibrational level of C_2H_2. In our externally irradiated models, the majority of the C_2H_2 emission region lies within this temperature regime (Figures 11 and C1). However, this pure IR-pumping population ratio calculation should (a) be compared directly to LTE level populations (rather than be taken as a representative value of n_1/n_0) and (b) include collisions. On the other hand, S. Bruderer et al. (2015) show that radiative pumping by a diluted blackbody dominates over collisional excitation. Thus, including the dilution factor (w) in Equation (F1), we obtain

$$\frac{n_1}{n_0} = \frac{g_1}{g_0} \frac{w}{\exp\left(\frac{1.44\,\tilde{\nu}}{T_{\rm rad}}\right) - 1}. \tag{F3}$$

To calculate the LTE level population ratio between the first excited vibrational state and the ground state, we assume that, in the LTE regime, the gas temperature equals the kinetic temperature ($T_{\rm kin} = T_{\rm gas}$). The population ratio is then

given by

$$\frac{n_1}{n_0} = \frac{g_1}{g_0}\frac{1}{\exp\left(\frac{h\nu}{kT_{\rm kin}}\right)}. \tag{F4}$$

For the non-LTE two-level population ratio, we perform a first-order approximation. We seek to calculate the population ratio n_1/n_0 between an upper level 1 and a lower level 0 in the presence of both radiation (IR pumping) and collisional excitation and de-excitation. The total excitation rate from $0 \rightarrow 1$ includes radiative excitation ($B_{01}\bar{J}_\nu$) and collisional excitation ($n_{\rm H_2}C_{01}$). The total de-excitation rate from $1 \rightarrow 0$ includes spontaneous emission (A_{10}), stimulated emission ($B_{10}\bar{J}_\nu$), and collisional de-excitation ($n_{\rm H2}C_{10}$). Solving for n_1/n_0 under statistical equilibrium, the upward and downward transition rates are given by

$$\frac{n_1}{n_0} = \frac{B_{01}\bar{J}_\nu + n_{\rm H_2}C_{01}}{A_{10} + B_{10}\bar{J}_\nu + n_{\rm H_2}C_{10}}. \tag{F5}$$

Now, from the Einstein relations, we know that

$$\frac{g_0 B_{01}}{g_1 B_{10}} = 1 \quad \text{and} \quad \frac{B_{01}}{A_{10}} = \frac{c^2}{2h\nu^3},$$

and, defining the photon occupation number as $\epsilon \equiv (e^{h\nu/kT_{\rm rad}} - 1)^{-1}$, we obtain

$$B_{01}\bar{J}_\nu = B_{01}\frac{2h\nu^3}{c^2}\epsilon = A_{10}\epsilon.$$

From the detailed balance of collisions, we have

$$C_{01} = C_{10}\frac{g_1}{g_0}e^{-h\nu/kT_{\rm kin}}.$$

Combining these expressions, we can compute the LTE/non-LTE population ratio. Expressed in terms of the wavenumber [$\rm cm^{-1}$], and including the dilution factor, we obtain

$$\frac{n_1}{n_0} = \frac{\left(\frac{g_1}{g_0}\right)\left[A_{10}\left(\frac{w}{e^{1.44\tilde{\nu}/T_{\rm rad}}-1}\right) + n_{\rm H2}C_{10}\left(\frac{g_1}{g_0}\right)e^{-1.44\tilde{\nu}/T_{\rm kin}}\right]}{A_{10}\left(1 + \frac{w}{e^{1.44\tilde{\nu}/T_{\rm rad}}-1}\right) + n_{\rm H2}C_{10}}. \tag{F6}$$

Since $A_{\rm ul}$ and $C_{\rm ul}$ for the molecules C_2H_2 and HCN are unknown, we adopt a value of $A_{10} \sim 10^{-2}$ [$\rm s^{-1}$], estimated using the ν^2 scaling of the electric dipole transition probability

$$A_{\rm ul} = \frac{64\pi^4\nu^3}{3hc^3}|\mu_{\rm ul}|^2,$$

where $\nu \sim 10^{13}$ Hz (MIR) and $|\mu_{\rm ul}| \sim 0.1 - 1$ D. For C_{10}, we adopt $C_{10} \approx 10^{-13}$ [$\rm cm^3\,s^{-1}$], since A. Faure & E. Josselin (2008) and D. Flower (2012) report values of the same order of magnitude for H_2O and CO, respectively, using H_2 as the collisional partner. Finally, these values of A_{10} and C_{10} imply a critical density of $n_{\rm crit} \approx 10^{11}$ [$\rm cm^{-3}$].

ORCID iDs

Sebastian Hernández Arboleda https://orcid.org/0009-0003-3793-2020
Germán Chaparro https://orcid.org/0000-0003-0919-1512
Pablo Cuartas-Restrepo https://orcid.org/0000-0002-5398-8265
Inga Kamp https://orcid.org/0000-0001-7455-5349
María Claudia Ramírez-Tannus https://orcid.org/0000-0001-9698-4080
Arjan Bik https://orcid.org/0000-0001-8068-0891
Jenny Frediani https://orcid.org/0009-0003-7663-5280
Thomas Haworth https://orcid.org/0000-0002-9593-7618
Thomas Henning https://orcid.org/0000-0002-1493-300X
Michael A. Kuhn https://orcid.org/0000-0002-0631-7514
Thomas Preibisch https://orcid.org/0000-0003-3130-7796
Bayron Portilla-Revelo https://orcid.org/0000-0002-6278-9006
Elena Sabbi https://orcid.org/0000-0003-2954-7643
Veronica Roccatagliata https://orcid.org/0000-0002-4650-594X
Sierk E. van Terwisga https://orcid.org/0000-0002-1284-5831
Andrew Winter https://orcid.org/0000-0002-7501-9801

References

Acke, B., Bouwman, J., Juhász, A., et al. 2010, ApJ, 718, 558
Acke, B., Van Den Ancker, M., Dullemond, C., Van Boekel, R., & Waters, L. 2004, A&A, 422, 621
Adams, F. C., Hollenbach, D., Laughlin, G., & Gorti, U. 2004, ApJ, 611, 360
Aléon, J., Lévy, D., Aléon-Toppani, A., et al. 2022, NatAs, 6, 458
Allen, M., Anania, R., Andersen, M., et al. 2025, OJAp, 8, 54
Ansdell, M., Haworth, T. J., Williams, J. P., et al. 2020, AJ, 160, 248
Ansdell, M., Williams, J. P., Manara, C. F., et al. 2017, AJ, 153, 240
Antonelli, M. A., Kim, S.-T., Peters, M., et al. 2014, PNAS, 111, 17749
Antonellini, S., Kamp, I., Riviere-Marichalar, P., et al. 2015, A&A, 582, A105
Aru, M.-L., Mauco, K., Manara, C. F., et al. 2024, A&A, 687, A93
Ballering, N. P., Cleeves, L. I., Haworth, T. J., et al. 2023, ApJ, 954, 127
Banzatti, A., Salyk, C., Pontoppidan, K. M., et al. 2025, AJ, 169, 165
Bate, M. R. 2018, MNRAS, 475, 5618
Berné, O., Habart, E., Peeters, E., et al. 2024, Sci, 383, 988
Bockelée-Morvan, D., Calmonte, U., Charnley, S., et al. 2015, SSRv, 197, 47
Boyden, R. D., & Eisner, J. A. 2020, ApJ, 894, 74
Bruderer, S., Harsono, D., & Van Dishoeck, E. F. 2015, A&A, 575, A94
Calahan, J. K., Öberg, K., & Booth, A. 2025, ApJ, 991, 94
Caro, G. M., Ruiterkamp, R., Schutte, W., Greenberg, J., & Mennella, V. 2001, A&A, 367, 347
Chaparro Molano, G., & Kamp, I. 2012a, A&A, 537, A138
Chaparro Molano, G., & Kamp, I. 2012b, A&A, 547, A7
Chown, R., Sidhu, A., Peeters, E., et al. 2024, A&A, 685, A75
Clarke, C. J. 2007, MNRAS, 376, 1350
Coleman, G. A., & Haworth, T. J. 2022, MNRAS, 514, 2315
Coleman, G. A., Mroueh, J. K., & Haworth, T. J. 2024, MNRAS, 527, 7588
Colmenares, M. J., Bergin, E. A., Salyk, C., et al. 2024, ApJ, 977, 173
Concha-Ramírez, F., Wilhelm, M. J. C., Portegies Zwart, S., & Haworth, T. J. 2019, MNRAS, 490, 5678
Cruz-Diaz, G. A., Ricca, A., & Mattioda, A. L. 2020, ESC, 4, 1730
Cuello, N., Dipierro, G., Mentiplay, D., et al. 2018, MNRAS, 483, 4114
Daffern-Powell, E. C., Parker, R. J., & Quanz, S. P. 2022, MNRAS, 514, 920
Daniel, F., Dubernet, M.-L., & Grosjean, A. 2011, A&A, 536, A76
Dere, K., Landi, E., Mason, H., Fossi, B. M., & Young, P. 1997, A&AS, 125, 149
Desch, S. 2007, ApJ, 671, 878
Facchini, S., Clarke, C. J., & Bisbas, T. G. 2016, MNRAS, 457, 3593
Fang, M., Van Boekel, R., King, R. R., et al. 2012, A&A, 539, A119
Faure, A., & Josselin, E. 2008, A&A, 492, 257
Feigelson, E. D., Townsley, L. K., Broos, P. S., et al. 2013, ApJS, 209, 26
Flower, D. 2012, MNRAS, 425, 1350
Frediani, J., Bik, A., Ramírez-Tannus, M. C., et al. 2025, A&A, 701, A14
Furlan, E., Watson, D. M., McClure, M., et al. 2009, ApJ, 703, 1964
Gárate, M., Pinilla, P., Haworth, T. J., & Facchini, S. 2024, A&A, 681, A84
Gaudi, B. S., Meyer, M., & Christiansen, J. 2021, ExoFrontiers: Big Questions in Exoplanetary Science (IOP Publishing), 2
Geers, V. C., Augereau, J.-C., Pontoppidan, K. M., et al. 2006, A&A, 459, 545
Gordon, I. E., Rothman, L. S., Hargreaves, R., et al. 2022, JQSRT, 277, 107949

Haworth, T. J., Kim, J. S., Winter, A. J., et al. 2021, MNRAS, 501, 3502
Henning, T., Kamp, I., Samland, M., et al. 2024, PASP, 136, 054302
Hester, J. J., Desch, S. J., Healy, K. R., & Leshin, L. A. 2004, Sci, 304, 1116
Hollenbach, D., Johnstone, D., Lizano, S., & Shu, F. 1994, ApJ, 428, 654
Joblin, C., & Tielens, A. G. G. M. 2020, PAHs and the Universe (EDP Sciences) doi:10.1051/978-2-7598-2482-3
Johnstone, D., Hollenbach, D., & Bally, J. 1998, ApJ, 499, 758
Kamp, I., Thi, W.-F., Woitke, P., et al. 2017, A&A, 607, A41
Kamp, I., Tilling, I., Woitke, P., Thi, W.-F., & Hogerheijde, M. 2010, A&A, 510, A18
Kanwar, J., Kamp, I., Woitke, P., et al. 2024, A&A, 681, A22
Kim, J. S., Clarke, C. J., Fang, M., & Facchini, S. 2016, ApJL, 826, L15
Kóspál, Á., Ábrahám, P., Diehl, L., et al. 2023, ApJL, 945, L7
Kuffmeier, M., Zhao, B., & Caselli, P. 2020, A&A, 639, A86
Kusaka, T., Nakano, T., & Hayashi, C. 1970, PThPh, 44, 1580
Lange, K., Dominik, C., & Tielens, A. G. G. M. 2021, A&A, 653, A21
Lefèvre, C., Pagani, L., Juvela, M., et al. 2014, A&A, 572, A20
Manara, C. F., Ansdell, M., Rosotti, G. P., et al. 2023, in ASPC, 534
Mann, R. K., Di Francesco, J., Johnstone, D., et al. 2014, ApJ, 784, 82
Molano, G. C., Bautista, F., & Miguel, Y. 2018, IAUS, 14, 152
Nicholson, R. B., Parker, R. J., Church, R. P., et al. 2019, MNRAS, 485, 4893
Öberg, K. I., Boogert, A. A., Pontoppidan, K. M., et al. 2011, ApJ, 740, 109
O'Dell, C., & Wen, Z. 1994, ApJ, 436, 194
O'Dell, C., Wen, Z., Hu, X., et al. 1993, ApJ, 410, 696
Parker, R. J. 2020, RSOS, 7, 201271
Parker, R. J., Nicholson, R. B., & Alcock, H. L. 2021, MNRAS, 502, 2665
Pascucci, I., Herczeg, G., Carr, J., & Bruderer, S. 2013, ApJ, 779, 178
Pfalzner, S., Steinhausen, M., & Menten, K. 2014, ApJL, 793, L34
Portilla-Revelo, B., Getman, K. V., Ramírez-Tannus, M. C., et al. 2025, ApJ, 985, 72
Povich, M. S., Stone, J. M., Churchwell, E., et al. 2007, ApJ, 660, 346
Qiao, L., Haworth, T. J., Sellek, A. D., & Ali, A. A. 2022, MNRAS, 512, 3788
Ramírez-Tannus, M. C., Bik, A., Cuijpers, L., et al. 2023, ApJL, 958, L30
Ramírez-Tannus, M. C., Bik, A., Getman, K. V., et al. 2025, A&A, 701, A139
Reiter, M., & Parker, R. J. 2022, EPJP, 137, 1071
Ricci, L., Robberto, M., & Soderblom, D. R. 2008, AJ, 136, 2136
Richert, A. J. W., Feigelson, E. D., Getman, K. V., & Kuhn, M. A. 2015, ApJ, 811, 10
Richert, A. J. W., Getman, K. V., Feigelson, E. D., et al. 2018, MNRAS, 477, 5191
Richling, S., & Yorke, H. W. 2000, ApJ, 539, 258
Roccatagliata, V., Bouwman, J., Henning, T., et al. 2011, ApJ, 733, 113
Romero-Mirza, C. E., Öberg, K. I., Banzatti, A., et al. 2024, ApJ, 964, 36
Salas, J., Bautista, F., & Chaparro, G. 2023, MNRAS, 518, 75
Salyk, C., Pontoppidan, K. M., Blake, G. A., Najita, J. R., & Carr, J. S. 2011, ApJ, 731, 130
Scally, A., & Clarke, C. 2001, MNRAS, 325, 449
Schöier, F. L., van der Tak, F. F., van Dishoeck, E. F., & Black, J. H. 2005, A&A, 432, 369
Stolte, A., Morris, M., Ghez, A., et al. 2010, ApJ, 718, 810
Störzer, H., & Hollenbach, D. 1999, ApJ, 515, 669
Thi, W., Lesur, G., Woitke, P., et al. 2019, A&A, 632, A44
Tielens, A. G. 2008, ARA&A, 46, 289
Toci, C., Lodato, G., Livio, F. G., Rosotti, G., & Trapman, L. 2023, MNRAS: Letters, 518, L69
Valegård, P.-G., Waters, L., & Dominik, C. 2021, A&A, 652, A133
van Dishoeck, E. F., Grant, S., Tabone, B., et al. 2023, FaDi, 245, 52
Van Terwisga, S. E., & Hacar, A. 2023, A&A, 673, L2
Vicente, S., Berne, O., Tielens, A. G. G. M., et al. 2013, ApJ, 765, L38
Visser, R., Geers, V. C., Dullemond, C. P., et al. 2007, A&A, 466, 229
Williams, J. P., & Cieza, L. A. 2011, ARA&A, 49, 67
Winn, J. N., & Fabrycky, D. C. 2015, ARA&A, 53, 409
Winter, A. J., Benisty, M., Shuai, L., et al. 2024, A&A, 691, A43
Winter, A. J., Clarke, C. J., Rosotti, G., et al. 2018, MNRAS, 478, 2700
Winter, A. J., & Haworth, T. J. 2022, EPJP, 137, 1132
Woitke, P., Kamp, I., Antonellini, S., et al. 2019, PASP, 131, 064301
Woitke, P., Kamp, I., & Thi, W.-F. 2009, A&A, 501, 383
Woitke, P., Min, M., Pinte, C., et al. 2016, A&A, 586, A103
Woitke, P., Min, M., Thi, W.-F., et al. 2018, A&A, 618, A57
Woitke, P., Riaz, B., Duchene, G., et al. 2011, A&A, 534, A44
Woodall, J., Agúndez, M., Markwick-Kemper, A., & Millar, T. 2007, A&A, 466, 1197
Zannese, M., Tabone, B., Habart, E., et al. 2024, NatAs, 8, 577